Meteorol Atmos Phys 000, 1–27 (2003)
DOI 10.1007/s00703-003-0050-y

Meteorology and Atmospheric Physics
Printed in Austria

[1] Department of Meteorology, University of Hawaii, Honolulu, HI
[2] Department of Marine Earth and Atmospheric Sciences, North Carolina State University

Cold-air cyclogenesis along the Gulf-Stream front: investigation of diabatic impacts on cyclone development, frontal structure, and track

S. Businger[1], **T. M. Graziano**[2,*], **M. L. Kaplan**[2], and **R. A. Rozumalski**[2,**]

With 24 Figures

Received January 10, 2002; revised November 27, 2002; accepted August 20, 2003
Published online: ● ●, 2003 © Springer-Verlag 2003

Summary

On 24–25 February 1989 a storm brought high winds and moderate to heavy snow to the U.S. East Coast. The storm is noteworthy for its rapid mesoscale development within a polar air mass at relatively low latitudes and for the difficulty experienced by operational NWP models and forecasters in predicting the storm's impact. This paper investigates the mesoscale structure and evolution of the cold-air cyclone through analysis of enhanced data sets collected during the Experiment on Rapidly Intensifying Cyclones over the Atlantic (ERICA). Results are presented from numerical sensitivity studies of the impact of diabatic heating on storm structure and track using the Mesoscale Atmospheric Simulation System (MASS) model.

The following conclusions are drawn from the research. Differential surface fluxes in the vicinity of the Gulf Stream led to the development of a well-defined baroclinic zone at low levels that extended parallel to the axis of the Gulf-Stream front. The baroclinic zone strengthened and assumed the characteristics of a shallow warm front as the cyclone matured. Enhanced cyclonic vorticity, moisture-flux convergence, clouds, and precipitation accompanied the front. Early in the event a series of shallow, thermally forced vortices of small wavelength (~200 km) formed along the baroclinic zone in the area of maximum surface-heat fluxes offshore of the Carolinas. Baroclinic instability associated with a vigorous short-wave trough aloft resulted in the outbreak of deep convection surrounding and rapid intensification of the northernmost vortex.

Numerical sensitivity experiments were conducted to investigate the non-linear response of the mass field to the convection. The results show that latent heating in deep convection surrounding the surface low produced a mesoscale height perturbation aloft. The subsequent acceleration of the flow aloft substantially increased the integrated mass divergence above the surface cyclone, leading to deepening on the scale observed. The observed track of the low followed the axis of the warm front, which in turn followed the axis of maximum SST gradient associated with the Gulf-Stream front. Accurate simulation of the storm track required a high-resolution, full-physics run that included high-resolution SST data in the initial condition and moisture nudging during the early hours of the simulation.

1. Introduction

On 24 February 1989 a small synoptic-scale cyclone formed along the mid-Atlantic coast within cold air following a cold frontal passage two days previous. This cyclone was significant not only for the heavy snow accumulations (Fig. 1) and high winds that accompanied it, but also for its low-latitude development entirely within a polar air mass. The previous day

* Current affiliation: NWS Office of Climate, Water, and Weather Services, 1325 East-West Highway, Silver Spring, MD 20910.
** Current affiliation: NWS UCAR/COMET, Boulder, CO 80307-3000.

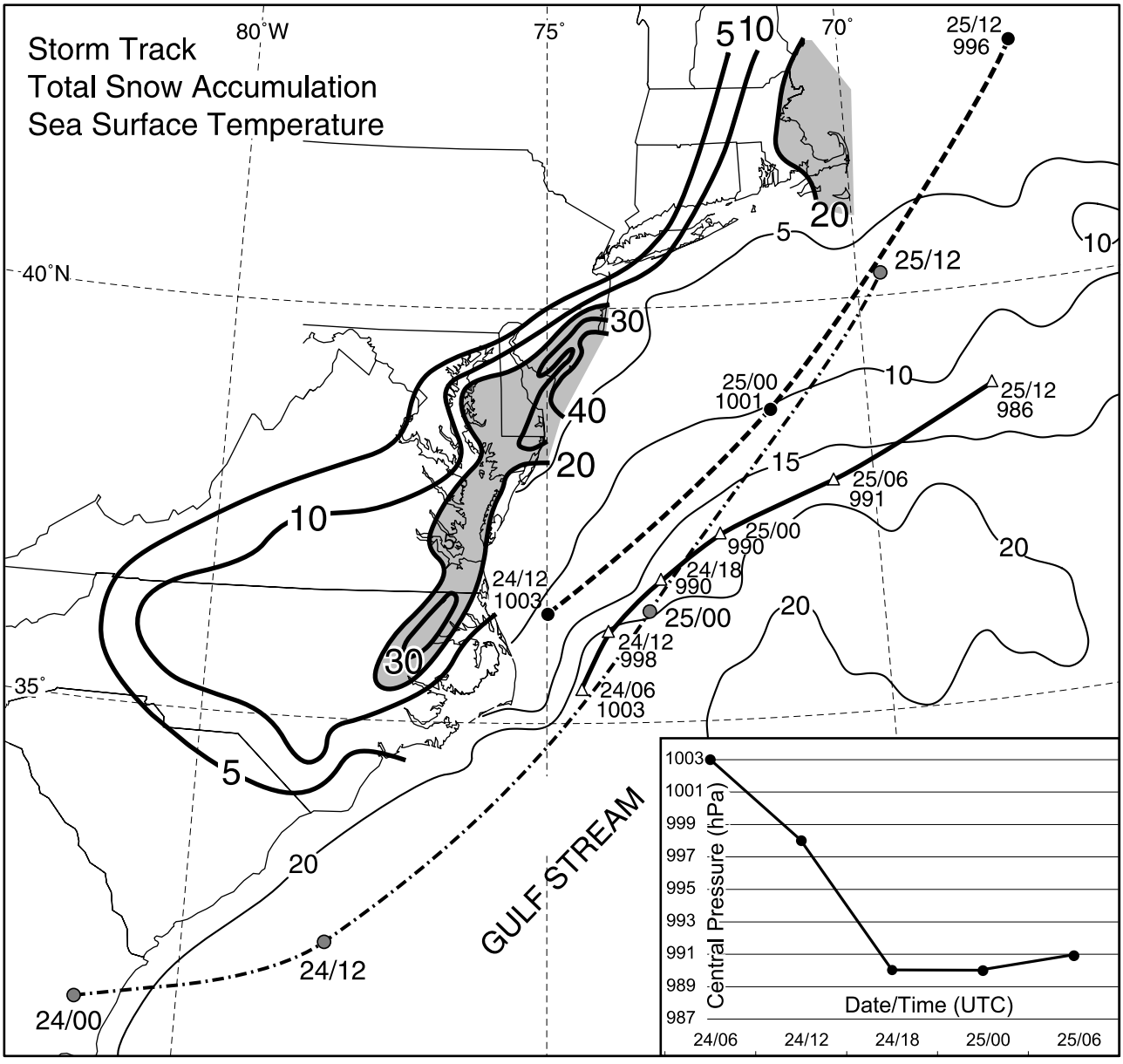

Fig. 1. Storm total snow accumulation (bold solid contours in cm, shaded areas >20 cm) from 23 February to 26 February 1989. Observed storm track: surface cyclone position (Heavy solid line, open triangles every 6 hours), 500-hPa short-wave absolute vorticity maximum (dash-dot line, large shaded circles every 12 hours), and storm track predicted by the NCEP's Nested Grid Model (heavy dashed line, solid circles every 12 hours). Thin solid contours over Atlantic Ocean are sea-surface isotherms (every 5 °C). Insert: Storm central pressure (hPa) with time on 24–25 February 1989

forecasters correctly anticipated a major coastal storm and issued a forecast for significant snow over the New York metropolitan area for 24 February; however, none actually fell in the immediate New York City area (Gigi, 1989). In large part this was because of an error in the storm track predicted by the NCEP's Nested Grid Model (NGM) (Fig. 1). This paper will investigate the evolution and structure of this unusual storm system with the benefit of enhanced observations taken during the Experiment on Rapidly Intensifying Cyclones over the Atlantic (ERICA) field experiment (Hadlock and Krietzberg, 1988).

Previous research has investigated the development of mesoscale vortices that form along the mid-Atlantic coast during cold-air outbreaks (Rosenblum and Sanders, 1974; Lin, 1989; 1990; Wayland and Raman, 1989; Warner et al, 1990;

Huang and Raman, 1991; 1992; Doyle and Warner, 1993). The relatively weak and shallow circulations form in response to shear instability, differential latent heating, and stretching of cyclonic vorticity along a shallow baroclinic zone or coastal front. In the present case shallow vortices were also observed over the Gulf Stream front; however, deep convection and rapid cyclogenesis (Fig. 1 inset) ensued with the approach of a cold-core low aloft. The small scale of the cyclogenesis and its development in a polar air mass suggest comparisons to polar lows, which commonly develop at higher latitudes (Rasmussen, 1981; 1985). For example, Businger (1985) shows that there is a propensity for mesoscale cyclogenesis to occur in polar air masses under synoptic conditions that include vorticity-rich, cold lows aloft, and enhanced air-sea temperature contrasts in air flowing from snow- and ice-covered surfaces to open water. More recently, Albright et al (1995) investigated an interesting case of mesoscale cyclogenesis over Hudson Bay. Their sensitivity studies show that a combination of cold advection aloft, warming by surface fluxes, and the configuration and location of the ice boundary are important factors in development. They conclude that condensational heating in deep convection was the overwhelming cause of the intensification.

The objectives of this research are to (i) investigate the impact of diabatic processes on the rapid surface cyclogenesis in the cold air, (ii) document the mesoscale structures associated with the ERICA cold-air cyclone, and (iii) investigate the poorly forecast track taken by the storm. To satisfy these objectives, detailed analyses of observational data and results of from numerical sensitivity experiments conducted using the Mesoscale Atmospheric Simulation System (MASS) model are presented.

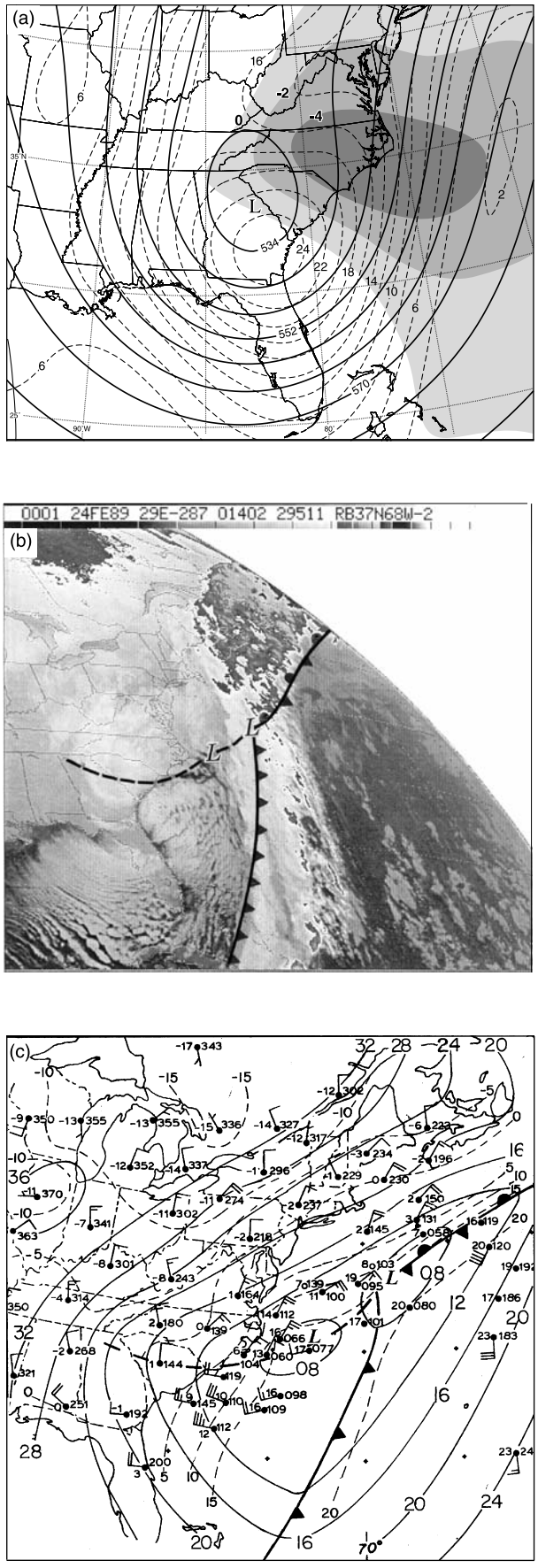

Fig. 2. Analyses for 0000 UTC 24 February; (**a**) Objectively analyzed 500 hPa geopotential height (solid contours every 60 m), vorticity (dashed contours every $2 \times 10^{-5}\ s^{-1}$), and omega fields (negative values shaded every $2\ hPa\ s^{-1}$); (**b**) GOES infrared satellite imagery; (**c**) sea-level pressure (solid contours every 4 hPa) and temperature (dashed contours every 5 °C). Observed winds are plotted in standard meteorological notation

2. Synoptic environment

An overview of the synoptic environment is presented in this section to provide context for the mesoscale analyses that follow. The sea-level analyses presented in this section are subjective analyses utilizing all available ERICA observational data. The General Meteorological Package (GEMPAK, desJardins et al, 1992) software was used to create objective upper-air analyses of ERICA rawinsonde data. Global Optimal Interpolation (GOI) (National Oceanic and Atmospheric Administration [NOAA], 1985) data were used as a first-guess field over the Atlantic Ocean. A two-pass Barnes (1973) analysis was used to grid the upper air data at 1.5° × 1.5° over a domain that extends from 15° N, 110° W northeastward to 55° N, 45° W.

During the week of 20 February a long-wave trough of relatively large meridional amplitude established itself aloft over the eastern United States. Associated with this trough, a strong surface cold front passed across the eastern United States during 21–22 February and was offshore of the mid-Atlantic coast by 1200 UTC 23 February. A strong, blocking Azores high slowed the eastward movement of the front, especially between 30° and 40° N latitude where the front remained quasi-stationary ~600 km offshore. Over the U.S., east of the Mississippi River, a north–northeasterly surface flow brought subfreezing temperatures to the Gulf of Mexico coast.

At 0000 UTC on 24 February the 500-hPa analysis shows a deep meridional trough over the eastern United States, with a closed circulation over Georgia and a pool of cold air (T < −30 °C, not shown) crossing the Appalachians into the Carolina Piedmont (Fig. 2a). A region of enhanced positive vorticity advection (PVA) aloft is diagnosed over the Carolina coast ahead of the upper-level trough. A broad area of colder cloud tops (Fig. 2b) and 50 dBZ radar echoes with tops extending to ~6.2 km (NOAA radar summary, not shown) were observed over the eastern half of North Carolina, coinciding with the area of enhanced upward motion seen in Fig. 2a.

At the surface, a trough axis or shear line extends from a parent frontal wave offshore to the Appalachians (Fig. 2c). The shear line forms the boundary between a cool north–northeasterly flow originating over New England and the Canadian Maritimes and a westerly flow over

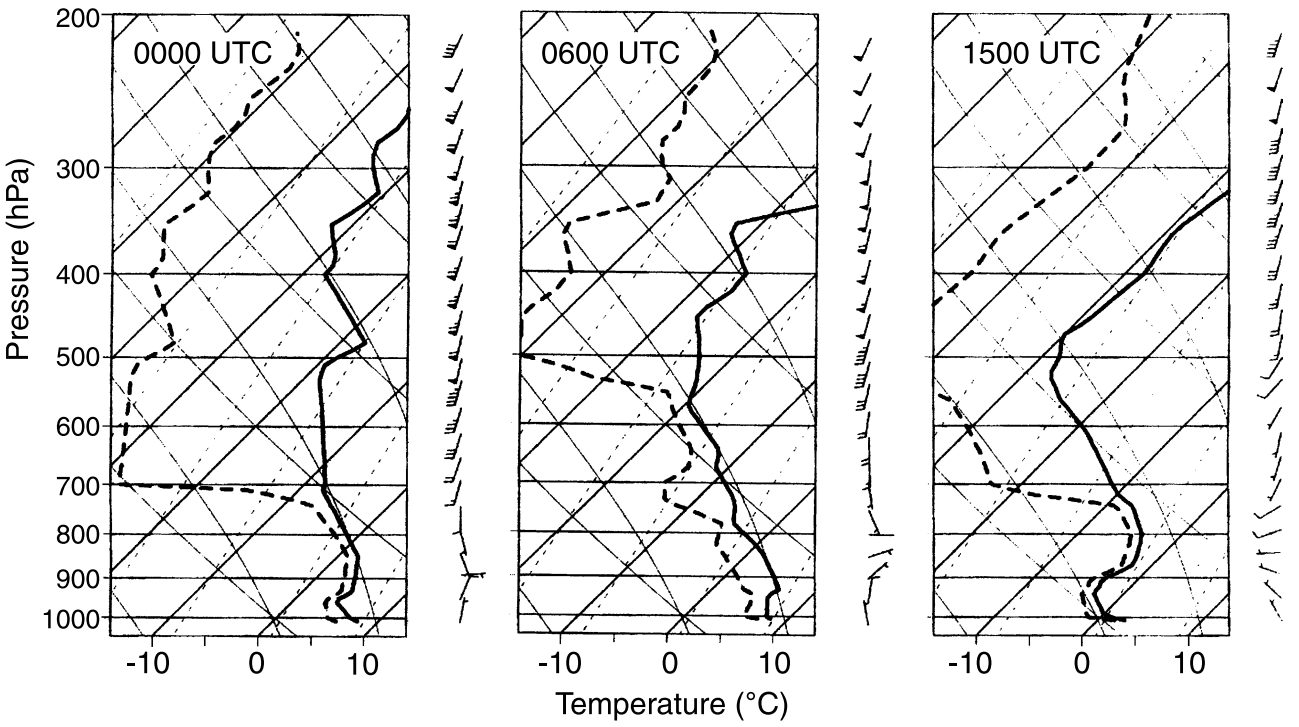

Fig. 3. Hatteras (72304, HAT) skew-T, log-p diagrams for 0000, 0600 and 1500 UTC 24 February 1989. Temperature (dew point) is depicted by heavy solid (dashed) line. Wind barbs plotted in standard convention

Georgia and South Carolina. The position of the offshore segment of the shear line coincides with the northern boundary or wall of the Gulf Stream. The shear line remains quasi-stationary in this orientation during the following ∼18 hours, as a result of the surface low's propagation parallel to the Gulf-Stream front (Fig. 1). The evolution of cloud streets in satellite imagery (Fig. 2b) suggests significant diabatic heating of continental polar air as the outflow crosses the Gulf Stream.

During a six-hour period beginning 0000 UTC 24 February, significant cold advection is observed over the Carolina coast in the mid- and upper troposphere, associated with the advancing short wave and upper-tropospheric cold pool (Figs. 3 and 4a). Low static stability in the lower troposphere coupled with decreasing static stability above gives way to low static stability through the bulk of the troposphere by 0600 UTC (Fig. 3a and b). This destabilization is manifested in a broad area of convective snow showers observed by weather radar along the mid-Atlantic coast and immediately surrounding the developing cyclone (not shown) and coincides with the onset of rapid surface cyclogenesis at 0600 UTC 24 February (Fig. 1 inset). By 1500 UTC the tropopause has lowered to ∼500-hPa, where the temperature has cooled to −28 °C, but the static stability in the lower troposphere over Cape Hatteras has increased as a result of enhanced cold advection at low levels in the wake of the developing cyclone (Fig. 3c). The result is an elevated unstable layer above a shallow inversion.

The infrared satellite image at 1200 UTC 24 February shows a region of cold cloud tops (−33 °C > T > −40 °C) associated with convective snow showers along the mid-Atlantic coast in the area of upward motion (Fig. 4a and b). Surface observations and satellite data support the presence of active convection reaching the tropopause surrounding the low center at this time (supporting high-resolution satellite data and mesoscale analyses are presented in Sect. 3). Frontogenesis along the confluent shear line extending from the offshore wave cyclone to the cold air low has resulted in the formation of a well-defined baroclinic zone at low levels (Fig. 4c). The zone is analyzed as a stationary front at this time due in part to the slow motion

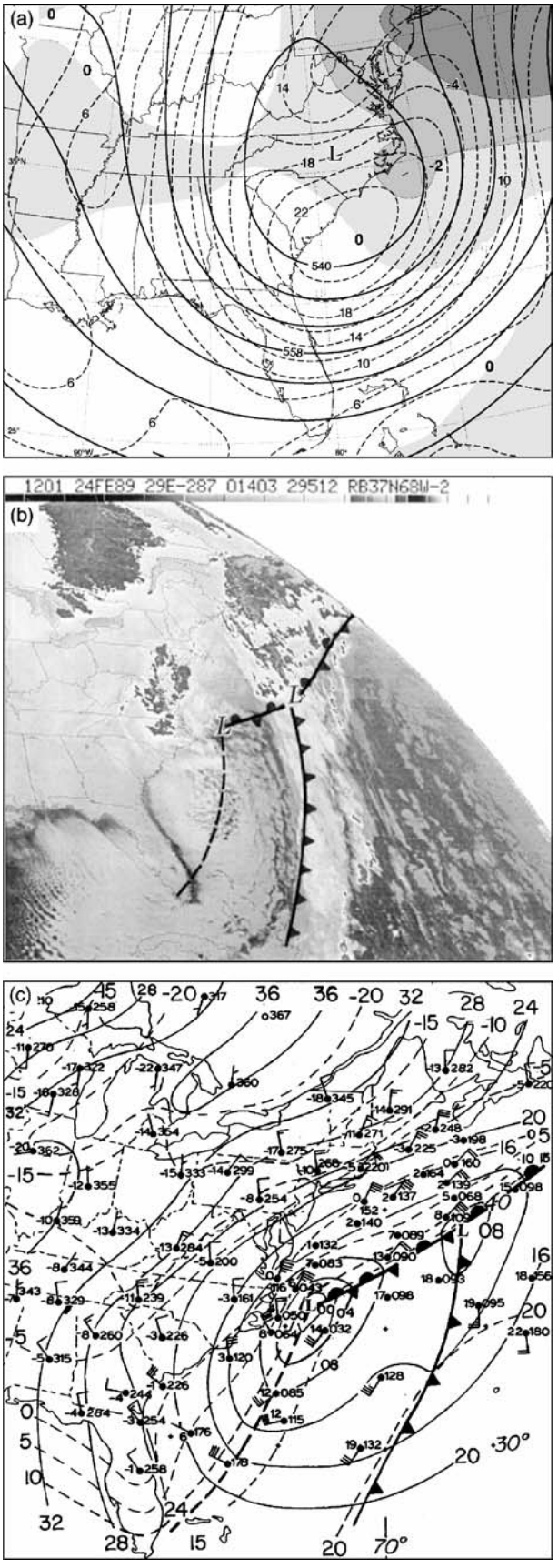

Fig. 4. As in Fig. 2 for 1200 UTC 24 February 1989

of the cold-air cyclone. South of the low, enhanced surface fluxes in the cold air are frontolytic.

The most rapid deepening rate of the central pressure of the cold-air cyclone occurred when the separation between the 500-hPa trough axis and the surface low center was ~550 km (Fig. 5a), consistent with B-type development (Petterssen and Smebye, 1971; Businger and Walter, 1988) and analytical results of Farrell (1984). Vertical profiles of the total divergence directly above the surface low center show that upper-level divergence is a maximum at the jet

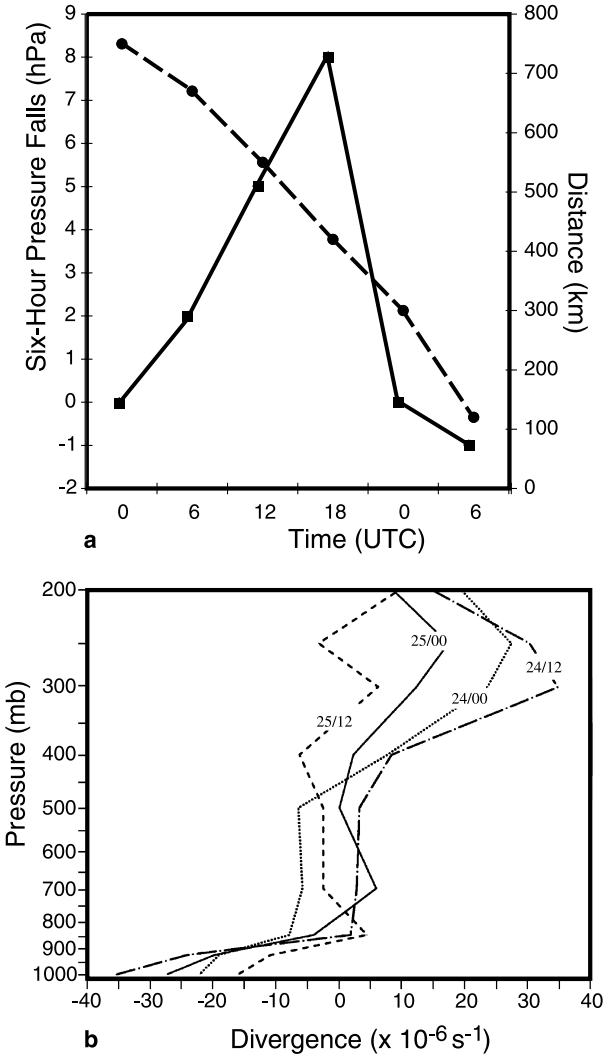

Fig. 5a. Six-hourly surface pressure falls (solid line) and distance between surface cyclone center and 500-hPa short-wave trough axis (dashed line) vs time (UTC) starting at 0000 UTC 24 February 1989; (**b**) Vertical profiles of the total divergence ($\times 10^{-6}\,s^{-1}$) above the surface low at 12-hourly intervals starting at 0000 UTC 24 February 1989

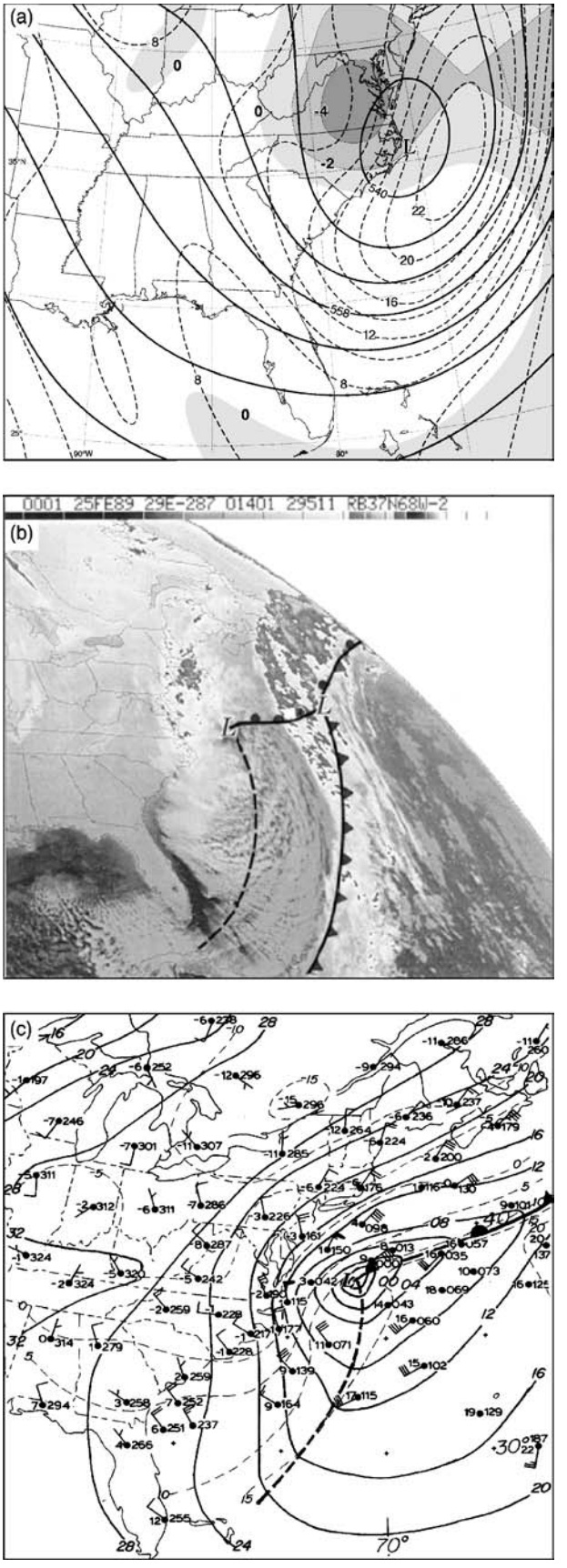

Fig. 6. As in Fig. 2 for 0000 UTC 25 February 1989

level at 1200 UTC 24 February (Fig. 5b). By 0000 UTC 25 February, the height, vorticity, and surface-low centers are nearly coincident (Fig. 6), with relatively weak 500-hPa positive vorticity advection over the cold-air cyclone. The surface low has deepened to ~990 hPa and has continued to propagate parallel to the Gulf Stream front (Figs. 1 and 6c). At this time the slow moving surface front is analyzed as a warm front, consistent with aircraft observations discussed in Sect. 3. Once the surface and 500 hPa low centers become vertically stacked, ending rapid development by upper-level baroclinic instability, the low's central pressure remained relatively steady on 25 February, deepening only 3 hPa to 986 by 1200 UTC (Fig. 1).

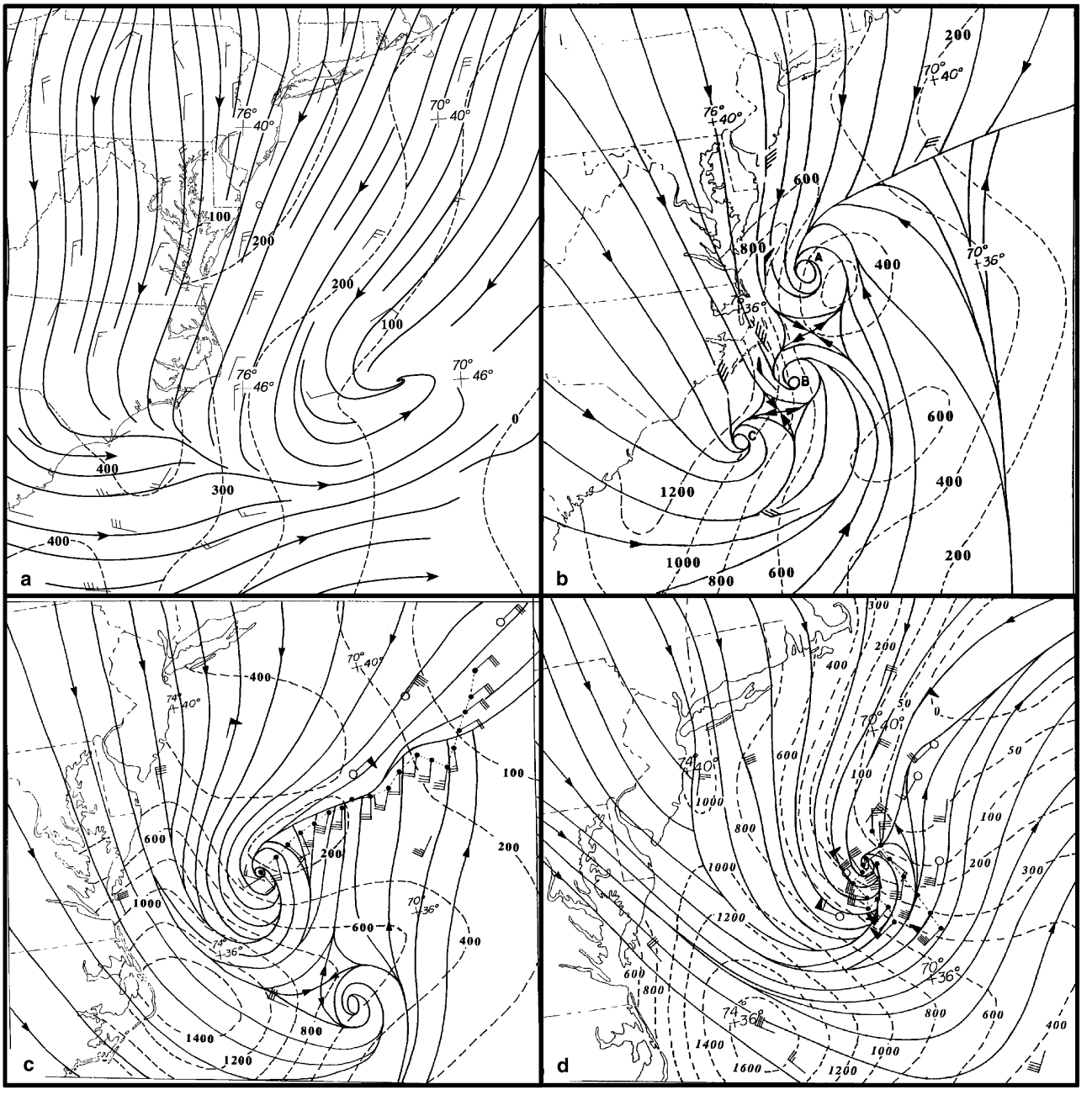

Fig. 7. Surface streamline analysis (solid lines) and total surface heat flux (W m^{-2}, dashed lines). Winds are plotted in standard convention. Valid for (**a**) 0000 24 February, (**b**) 1200 UTC 24 February, (**c**) 0000 25 February, (**d**) 0600 UTC 25 February 1989

2.1 Surface heat fluxes

Maximum air-sea temperature differences in this case exceeded 20 °C and air temperatures offshore were well below freezing, qualifying this event as an intense cold air outbreak (Grossman and Betts, 1990). To aid in evaluating the impact of diabatic warming and moistening of the marine boundary layer (MBL) on the structure and track of the storm, calculations of sensible and latent heat fluxes were made using the bulk aerodynamic method (Stull, 1993; Arya, 1988) (see Appendix). The analyses shown in Fig. 7 were constructed with the aid of all available ship and buoy reports, 300-m flight-level winds, and with reference to cloud fields in satellite imagery and high-resolution SST data (e.g., Fig. 1).

Early on 24 February, increasing winds and cold advection on the southwest side of the developing low led to an increase in maximum surface fluxes from ~400 to over 1200 W m^{-2} by 1200 UTC in the northwest flow along the Carolina coast (Fig. 7a and b). During this period, surface fluxes in the northeast flow on the north side of the low and developing stationary front were significantly less, ranging from 100 to 400 W m^{-2}. Shallow vortices formed in the wake of the strongest surface fluxes in Fig. 7b. These vortices and the deepening of the cloud elements in response to the surface heating can be seen off the Carolina coast in the DMSP satellite images for 1500 and 1740 UTC 24 February 1989 (Fig. 8).

The pattern of differential surface fluxes surrounding the low is accentuated at 0000 UTC on 25 February, with maximum fluxes >1400 W m^{-2} southwest of the mature low and between 100 and 200 W m^{-2} into the air just north of the warm front (Fig. 7c). The locations of sensible and latent heat-flux maxima coincide

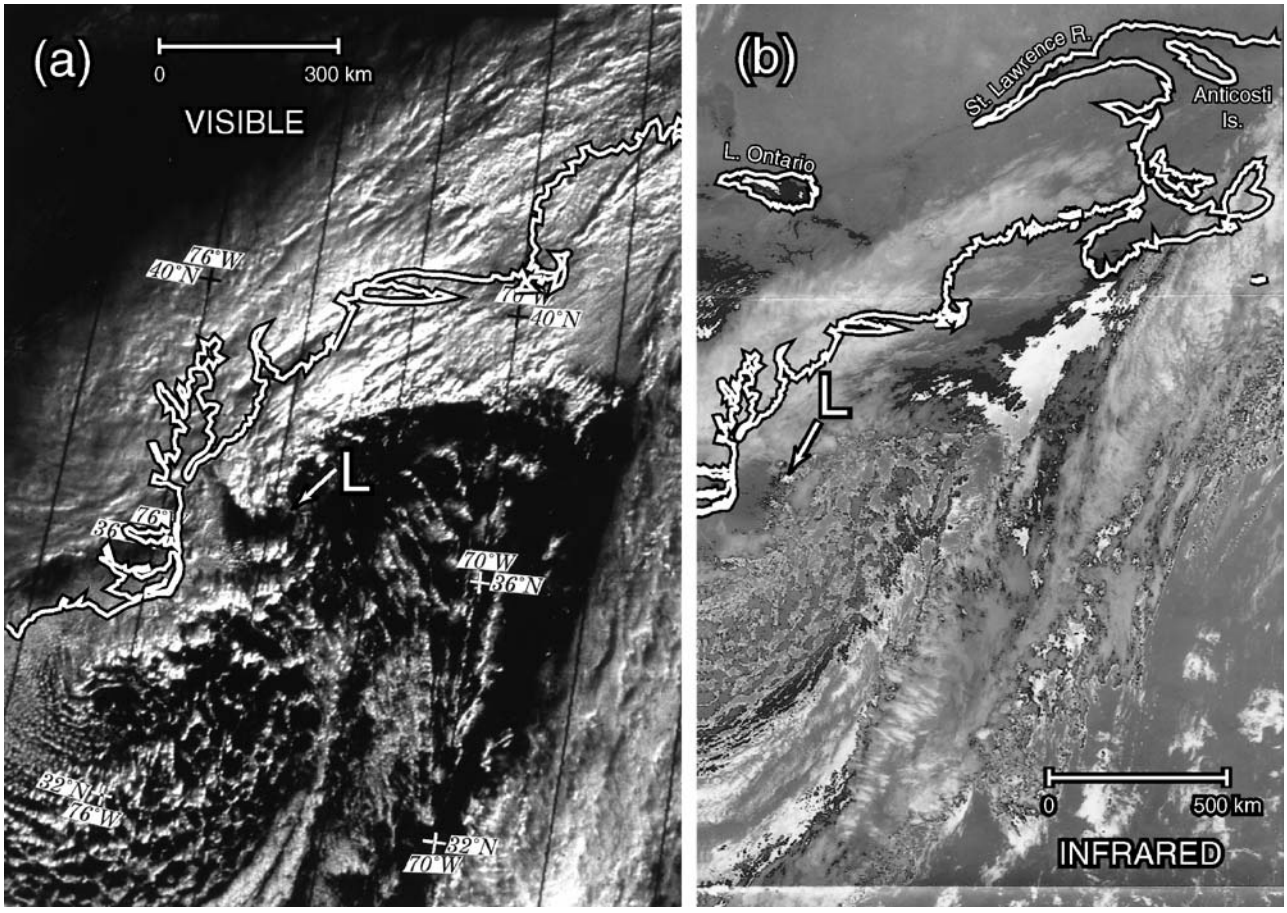

Fig. 8. Polar orbiting satellite imagery on 24 February 1989: (**a**) DMSP visible plus near infrared image for 1500 UTC; (**b**) NOAA 10 infrared image for 1740 UTC

and their relative contributions (not shown) remain nearly equal at 1200 UTC 24 February and 0000 UTC 25 February, a result that is consistent with previous findings (Shapiro et al, 1987; SethuRaman et al, 1986). The implication of this observation is that roughly half of the surface fluxes are sensible heat, which contributes directly to the development of low-level temperature gradients and destabilization of the lapse rate in the MBL. As a result of the distribution of surface heating, air parcels arriving at the warm front from the south will have a significantly different history of heating from those arriving at the north side of the warm front, contributing significantly to observed frontogenesis.

The region of surface heat fluxes up to $1000\,\mathrm{W\,m^{-2}}$ is within the confines of the western convergent asymptote and presumably contributes to the warmth at the core of the storm. By 0600 UTC on 25 February surface fluxes into air surrounding and ingested by the low have increased to $>1200\,\mathrm{W\,m^{-2}}$, with values $>1600\,\mathrm{W\,m^{-2}}$ farther to the southwest (Fig. 7d).

To explore the impact of surface heating on the track of the marine cyclone, we compute the potential thickness, defined as the 1000–500 hPa thickness that would result if the environmental lapse rate were modified to lie along a moist adiabat representing saturation at 1000 hPa and at the sea surface temperature (Davis and Emanuel, 1988). Figure 9 depicts the potential thickness anomaly; i.e., the difference between the potential thickness, computed using gridded one degree resolution AVHRR weekly composite sea-surface temperature data for 16 to 22 February 1989 and the analyzed 1000–500 hPa thickness. Conceptually, the potential thickness anomaly represents the difference between the upper limit to which the sea-surface fluxes can modify the overlying atmosphere and the observed atmospheric environment.

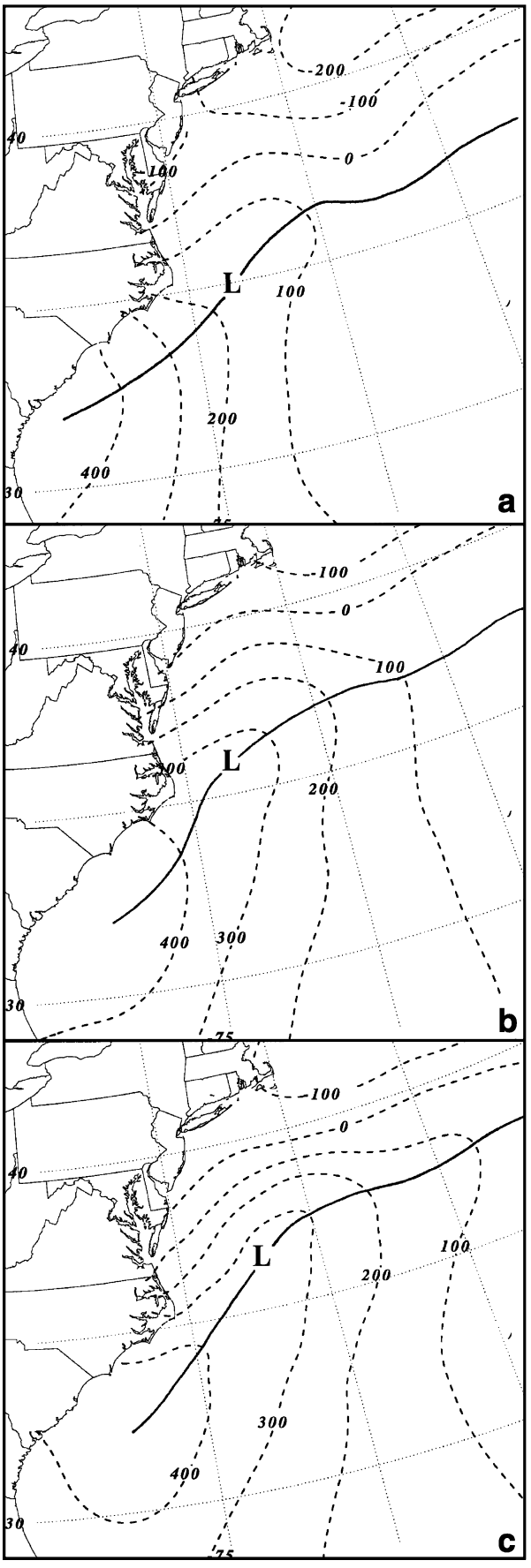

Fig. 9. Contours of potential thickness anomaly in meters (dashed line) for (**a**) 0000 UTC 24 February, (**b**) 1200 UTC 24 February, (**c**) 0000 UTC 25 February. The observed position of the surface cyclone is denoted by the "L." Axis of maximum potential thickness anomaly is depicted by solid line

The observed position of the surface low falls on the axis of maximum the potential-thickness anomaly for each synoptic time shown in Fig. 9. In the convective region near the low center the actual lapse rate will be closest to the theoretical lapse rate associated with the potential thickness, suggesting a link between the ability of sea-surface fluxes to modify the atmosphere and the location of the surface low. A similar result was found in the case of a polar low observed over the Bering Sea (Businger and Baik, 1991). Recall that the NGM forecast track was to the north of the observed track over colder water (Fig. 1).

3. Mesoscale analysis

Enhanced data sets available for the Intensive Operating Period (IOP) 8 of ERICA are used in this section to investigate the mesoscale structure of the cold-air cyclone. The first NOAA P-3 research-aircraft flight during IOP-8 tracked parallel to the quasi-stationary front on 24 February 1989. Sea-level pressures determined from flight-level measurements were integrated with the ship and buoy reports to construct the subjective sea-level pressure analysis valid for 1800 UTC 24 February (Fig. 10). The analysis shows an asymmetric pressure distribution, with the strongest pressure gradient to the north and west of the low center and a weaker gradient southeast of the low. Reconnaissance aircraft data estimate a central sea-level pressure of ~990 hPa, corresponding to a 13 hPa pressure fall during the 12-hour period ending at 1800 UTC. This pressure fall occurs over a relatively short period in the life of the cold-air cyclone.

Cross-sectional analysis using aircraft flight-level and dropsonde data at 1800 UTC on 24

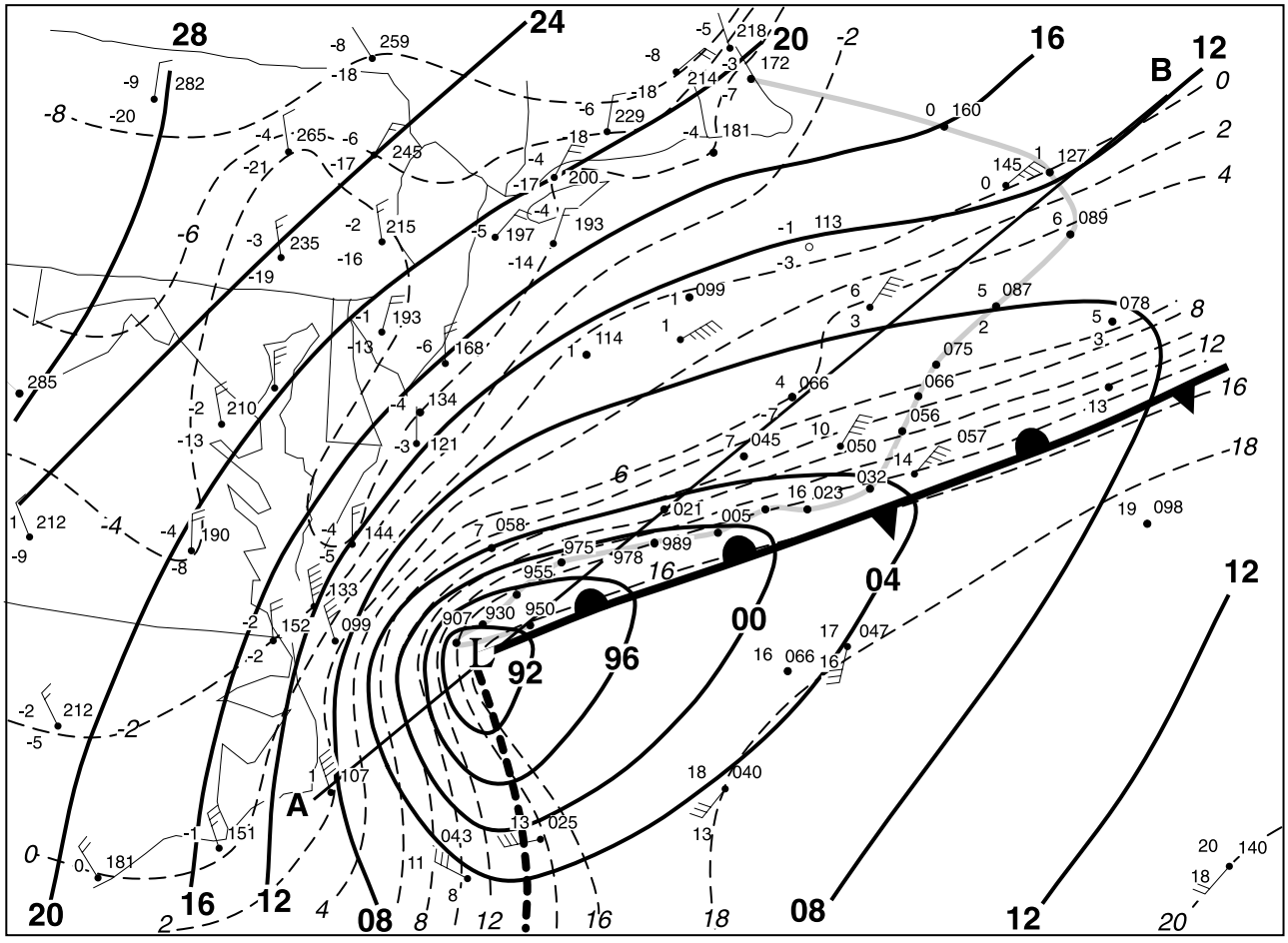

Fig. 10. Sea-level analysis of pressure (solid lines every 4 hPa) and temperature (dashed lines every 2 °C) for 1800 UTC 24 February. Aircraft track (gray line) and flight level data used in this analysis were time-distance adjusted for storm motion to 1800 UTC. Line A–B is the cross-section projection line of Fig. 11. Winds are plotted in standard convention

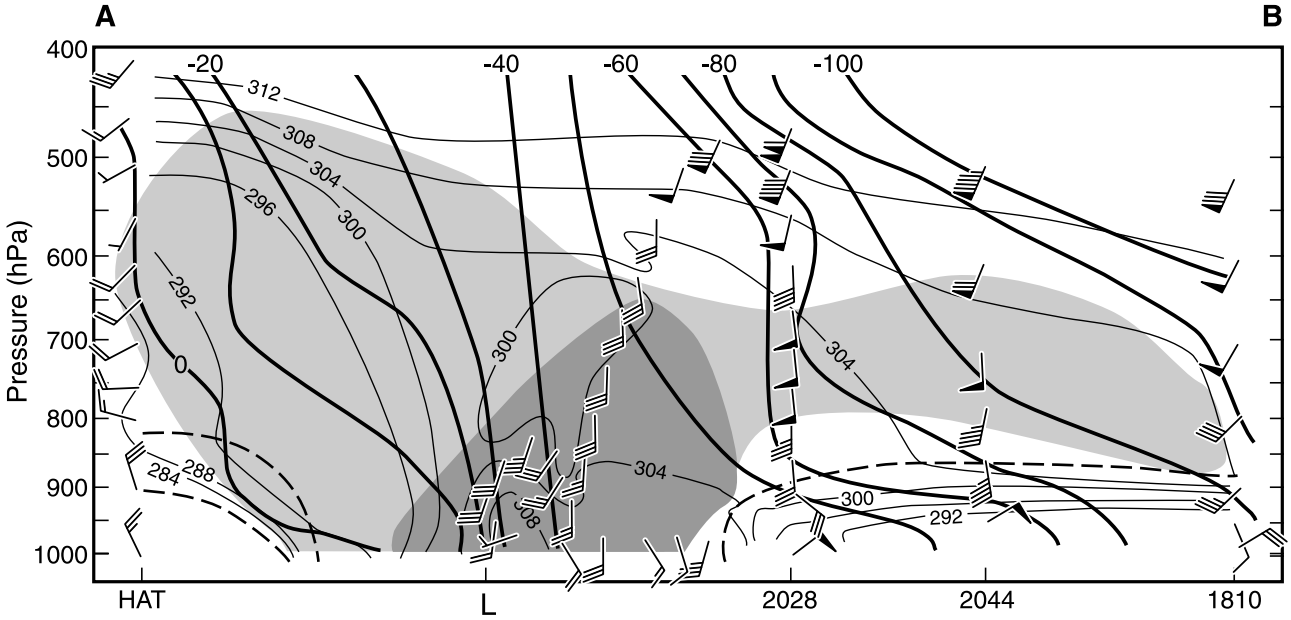

Fig. 11. Cross section showing absolute momentum (heavy lines every $10\,\mathrm{m\,s^{-1}}$) and equivalent potential temperature (thin lines every 4 K) for 1800 UTC 24 February along line A–B of Fig. 10. Stable layers and frontal boundaries are indicated by heavy dashed lines. Dropsondes are identified by release time (UTC) along the abscissa. Areas of conditional symmetric instability are shaded light. Dark shading indicates areas conditionally unstable to upright convection near the low center. Plotted winds are standard convention

February (Fig. 11) shows a sharp gradient in equivalent potential temperature, pronounced convergence, and cyclonic shear across the surface front. Surface winds just ahead of the front are from the south–southwest at $23\,\mathrm{m\,s^{-1}}$, whereas behind the front winds are northeast at $25\,\mathrm{m\,s^{-1}}$. Pronounced veering of the winds with height across a stable boundary layer inversion near 900 hPa just north of the surface frontal position indicates the structure is that of a shallow warm front. A gradual strengthening of the warm front is consistent with enhanced frontogenesis and moisture-flux convergence along the axis of the front.

Symmetric instability can be assessed in the atmosphere by determining the buoyancy of a parcel while following a surface of absolute momentum ($M = v + fx$) (Emanuel, 1983a). Absolute momentum surfaces at 1800 UTC reveal nearly vertical M surfaces, implying unstable conditions for upright convection in the near vicinity of the low center (Fig. 11). To the southwest of the surface low, the cross section A–B intersects a stable region associated with a shallow coastal front and the outflow of cold continental air. In this region slantwise overrunning of the continental air by more modified air from the west is symmetrically unstable to ~500 hPa in the vicinity of the convergence line (θe decreases following M contour in Fig. 11) (Sanders and Bosart, 1985). To the northeast of the surface low, the cross section becomes roughly parallel to the isotherms, and symmetric instability cannot accurately be diagnosed by this method but may have been present.

High-resolution visible plus near infrared imagery from the DMSP polar-orbiting satellite for 1500 UTC on 24 February (Fig. 8a) reveals a sharp cloud edge at the location of the strengthening warm front, separating a region of open-cell convection from overcast conditions with embedded convection to the north. This observation is consistent with the cross-section analysis in Fig. 11 and with the characterization the baroclinic zone as a warm front and axis of moisture flux convergence. Well-defined cloud elements characteristic of deep convection are seen over the Gulf-Stream front just off the North Carolina coast and surrounding the low. The cloud band seen along the right-hand side of the image is a stalled front associated with the preceding wave cyclone. High-resolution infrared imagery from the NOAA

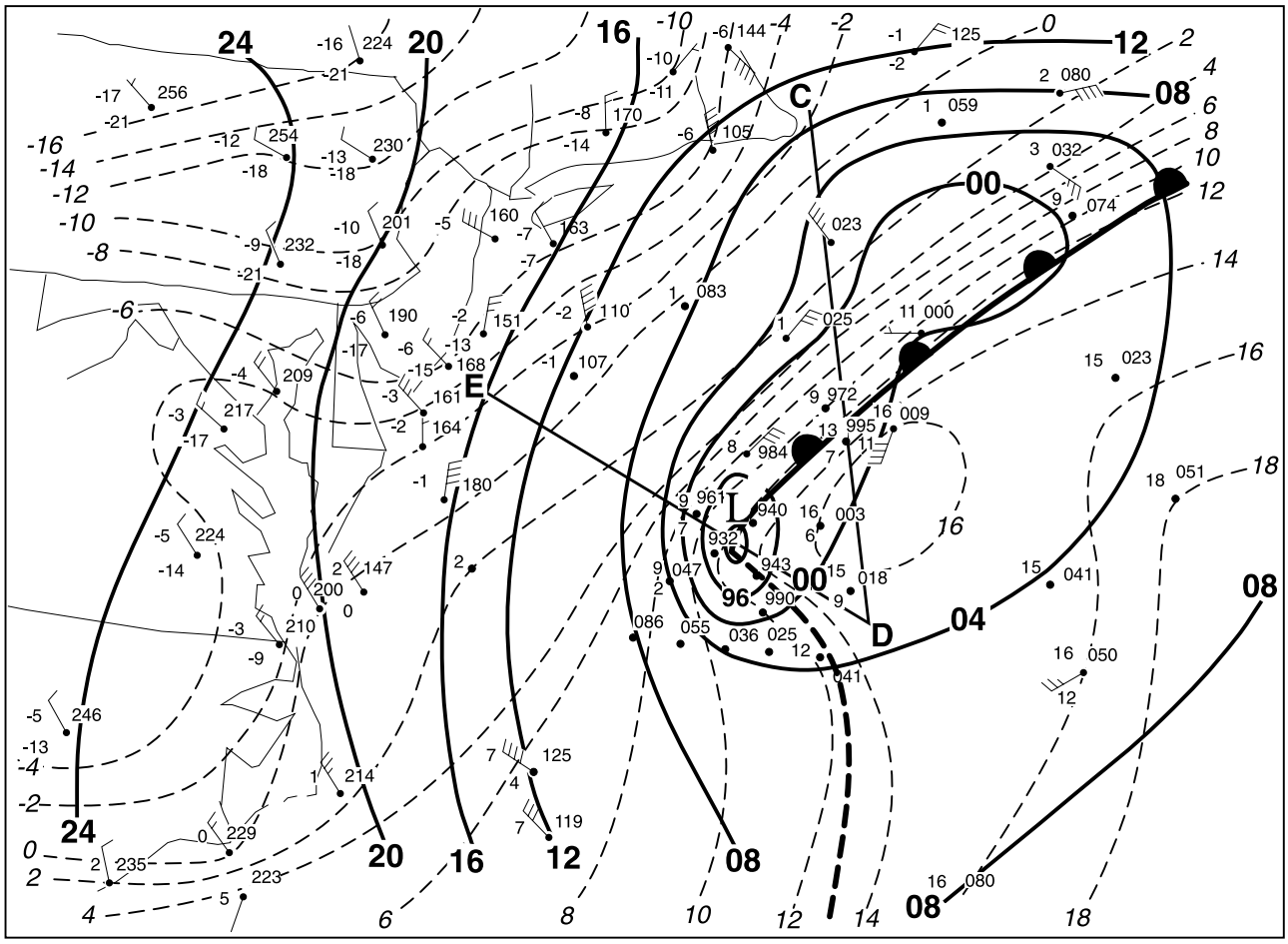

Fig. 12. Sea-level analysis for 0600 UTC 25 February 1989 of pressure (solid lines every 4 hPa) and temperature (dashed lines, °C). Winds plotted in standard convention. Flight-level data used in this analysis were time-distance adjusted for storm motion to 0600 UTC. Lines C–D, and E–D indicate the location of cross sections in Fig. 14

polar-orbiting satellite for 1741 UTC on 24 February (Fig. 8b) indicates deeper convection immediately surrounding the low center and in the cloud mass offshore from Boston to the Virginia Coast. Convective cloud top temperatures at this time are near −30 °C, corresponding to the tropopause in U.S. East Coast soundings (e.g., Fig. 3c).

The second penetration of the storm occurred ∼12 hours after the first. The estimated central pressure at 0600 UTC on 25 February had risen slightly from ∼990 to ∼991 hPa since the first aircraft penetration (Fig. 12). The surface analysis shows a more symmetric, tight pressure gradient and a region of enhanced winds near the core of the low.

The surface temperature analysis at 0600 UTC on 25 February shows a large temperature gradient across the warm front (Fig. 12), and a relatively weak gradient south of the low, where continental polar air is modified by surface fluxes after crossing the U.S. East Coast. A tongue of cooler air appears to have secluded warm air near the low center (Bergeron, 1928; Neiman and Shapiro, 1993).

Analysis of airborne radar data shows spiral bands of higher reflectivity (>40 dBz) with embedded convective cells surrounding an echo-free core region at the low center (Fig. 13). The tail radar range height indicator scan (not shown) reveals echo tops just SE of the low center extending to ∼4700 m (540 hPa), consistent with satellite estimates. High-resolution NOAA polar-orbiting satellite imagery at 1220 UTC on 25 February (Fig. 14) reveals a cloud-free cyclone core surrounded by active convective clouds near the center of the low, consistent with the radar data. GOES infrared imagery at 0601 UTC on

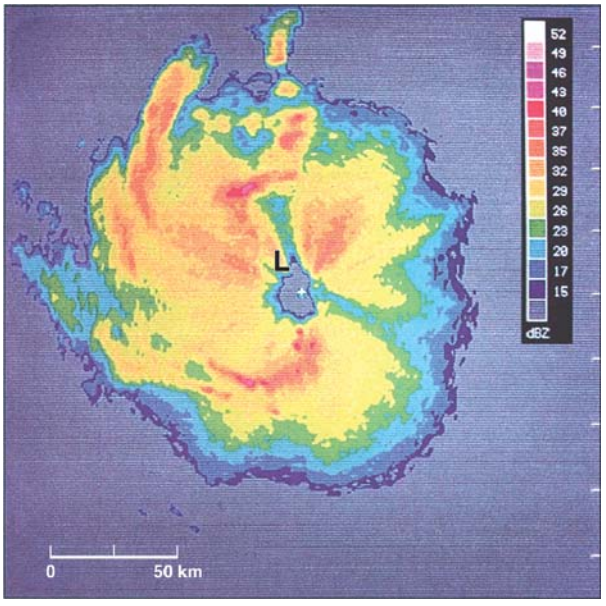

Fig. 13. NOAA P-3 airborne Doppler radar imagery for 0551 UTC 25 February 1989. The aircraft was located immediately SE of the cyclone center at 37.33° N and 70.66° W and heading southwestward. Plan Position Indicator (PPI) scan of echo intensity from lower fuselage radar. 240 × 240 km domain with tick marks on ordinate representing 24 km intervals. Reflectivity intensities (dBZ) are identified in the color bar

25 February (not shown) indicates a similar pattern of deep convection surrounding a cloud-free center region. Cloud top temperatures at 0600 UTC remain near −30 °C in the convective regions surrounding the low. The pattern of convection and the enhanced pressure gradient near the core of the low are similar to those observed in polar lows (Rasmussen, 1981; 1985; Businger and Baik, 1991) and the inner cores of some midlatitude cyclones (e.g., Nieman and Shapiro, 1993). Indirect evidence of enhanced surface fluxes is seen in the transition from clear air to cloud streets and open cell convection offshore of Cape Hatteras to the southwest of the low center, consistent with the surface flux calculations presented in Sect. 2.

The second NOAA P-3 flight crossed the mature low center at several levels allowing construction of a three-dimensional view of this mature stage in the storm. Cross-section C–D intersects the warm front and reveals a shallow, well-defined front capped by a strong stable layer (Fig. 15a and b). The frontal zone is characterized by substantial wind shear, with veering of

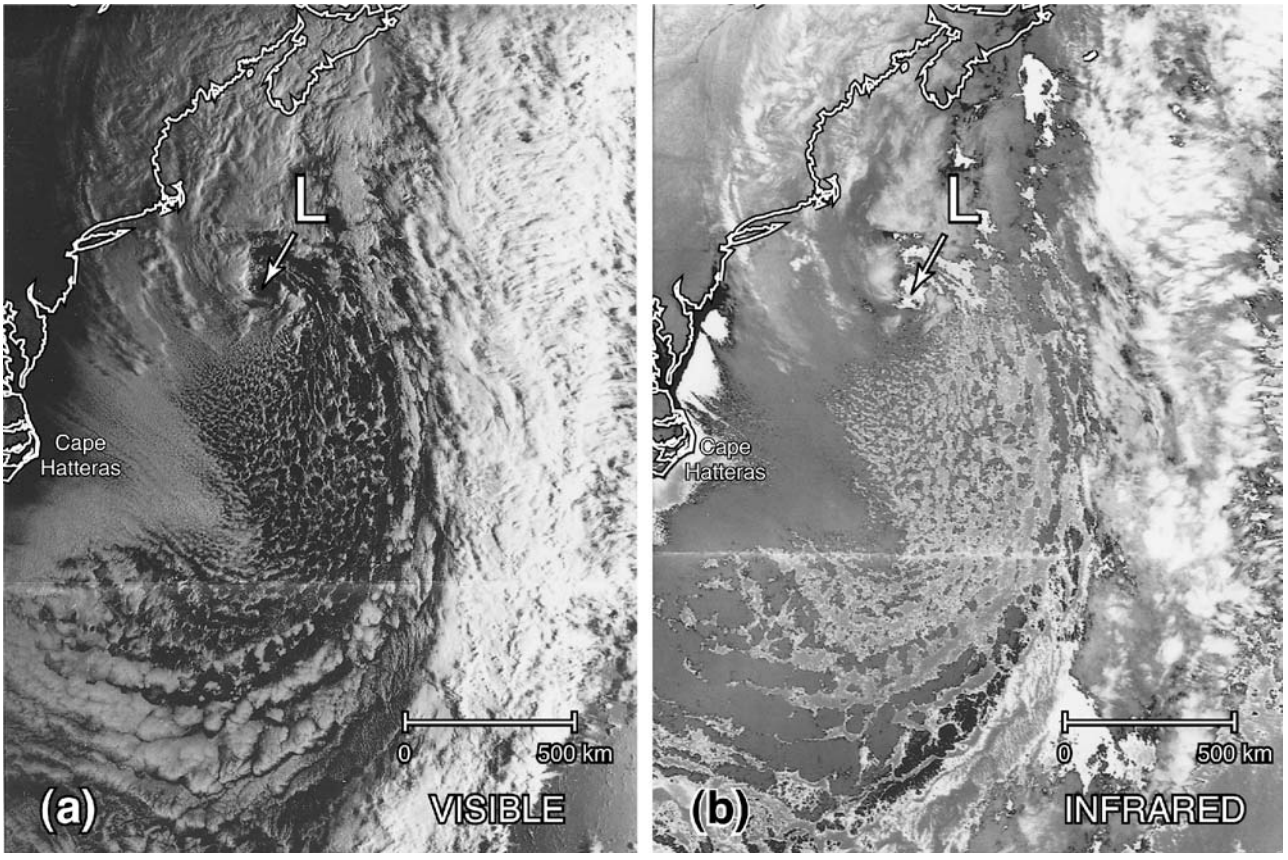

Fig. 14. NOAA 10 polar orbiting satellite imagery for 1220 UTC 25 February 1989: (**a**) visible, (**b**) infrared

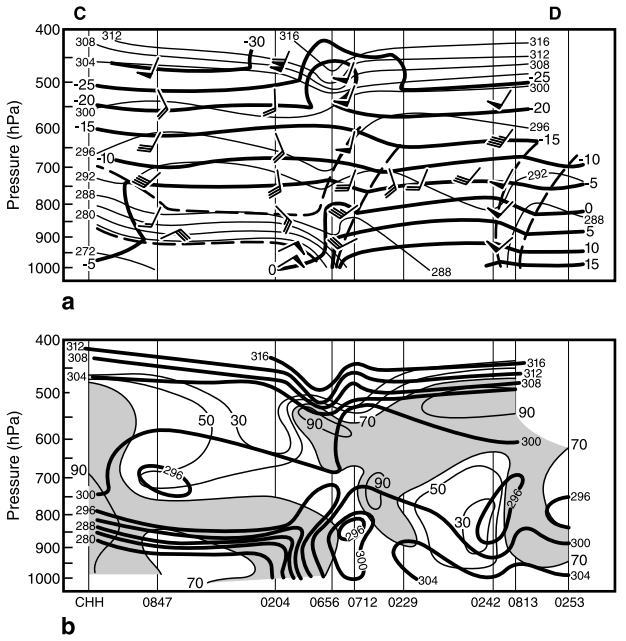

Fig. 15. Cross-section analysis for 0600 UTC 25 February 1989 along projection line C–D in Fig. 12; (**a**) Potential temperature (K, bold lines) and temperature (°C, thin solid lines). Stable layers and frontal boundaries are indicated by dashed lines, winds plotted in standard convention; (**b**) Equivalent potential temperature (K, bold lines) and relative humidity (%, thin lines)

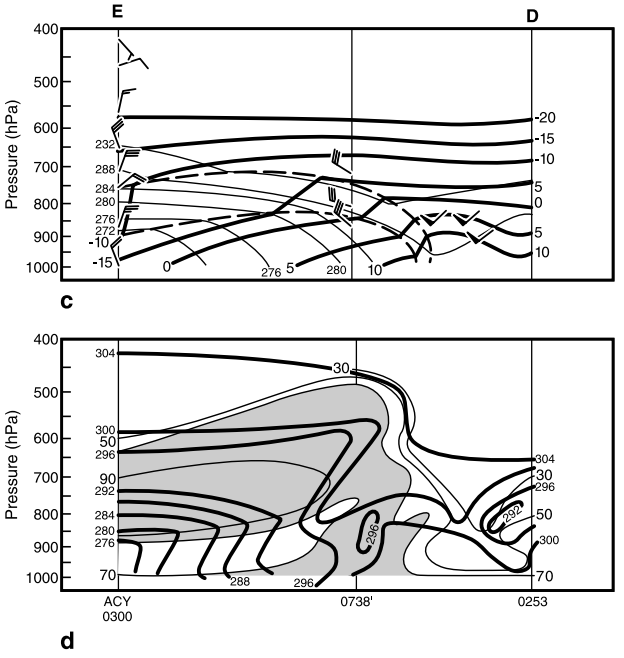

Fig. 15c and d (*continued*). As in 15a and b but along projection line E–D in Fig. 12

the winds indicative of a warm front (Fig. 15a). Above the frontal zone, which is confined below ~800 hPa, the atmosphere is conditionally unstable to a polar tropopause near 500 hPa (Fig. 15b).

Cross section E–D intersects the low and shows a warm core at low levels, with low static stability above (Fig. 15c and d). Boundary-layer winds exceed 25 m s^{-1} from the southwest on the southeast side of the low and from the northeast on the northwest side of the low (Fig. 15a and c), consistent with observations of a tight pressure gradient near the low center. Static stability is low above the circulation center and shallow convective instability exists on the cold-air side of the trough. Moisture analysis reveals a core region of high relative humidity above the low reaching to near 500 hPa (Fig. 15d), consistent with satellite and airborne Doppler radar data showing deep convection surrounding the low center.

4. Numerical sensitivity studies

Numerical sensitivity studies utilizing the MASS model presented in this section were performed to investigate the impact of latent heating and surface fluxes on the rapid cold-air cyclogenesis and cyclone track during ERICA IOP 8. Additionally, the link between mesoscale mass adjustments and convection are investigated to shed light on the mechanism behind the mesoscale cold-air cyclogenesis.

The MASS model is a hydrostatic, atmospheric primitive equation model with 7 prognostic variables: temperature, water vapor mixing ratio, u-wind component, v-wind component, pressure, cloud water/ice mixing ratio, and rainwater/snow mixing ratio (MESO, Inc., 1995). The original version of MASS (version 2.0) was developed by Kaplan et al (1982) and subsequently modified into the Goddard Mesoscale Atmospheric Simulation System (GMASS). Over the past two decades, the MASS model has been widely utilized in mesoscale modeling studies (Kaplan et al, 1982; Kocin et al, 1985; Koch et al, 1985; Koch, 1985; Uccellini et al, 1987; Zack and Kaplan, 1987; Whitaker et al, 1988; Cram et al, 1991; Manobianco et al, 1994; Kaplan and Karyampudi, 1992).

In recent years, improvements have been incorporated in later versions of the MASS model, which include the split-explicit time integration and prognostic grid scale moisture schemes, an enhanced surface-energy budget, a

Table 1. Experimental design

Description of simulation	Hourly nudging w/SFC observations	Hourly nudging w/MDR data	Surface fluxes	Latent heating	Horizontal grid resolution (true at 35° N)	Array size
Control full physics (w/nudging)	yes	yes	yes	yes	20 km	145 × 170
Full physics (no nudging)	no	no	yes	yes	20 km	145 × 170
No surface fluxes	yes	yes	no	yes	20 km	145 × 170
No latent heating	yes	no	yes	no	20 km	145 × 170
Adiabatic	yes	no	no	no	20 km	145 × 170
Coarse full physics (w/nudging)	yes	yes	yes	yes	60 km	49 × 57

modified Kuo cumulus parameterization scheme with moist downdraft physics, and a more comprehensive long and short wave radiation scheme (Manobianco et al, 1994; MESO, Inc., 1995). Additionally, the version of the MASS model (MASS 5.8) used in this research uses a recently implemented three-dimensional multivariate optimal interpolation (3-D OI) scheme in lieu of the Barnes (1973) objective analysis scheme. The modified Kuo convective parameterization scheme and Blackadar planetary boundary-layer scheme employed in our simulations both tend to bias the control simulation toward over-deepening the surface low-pressure center. However, this tendency offsets in part the inhibition of moist and dry convection by the relatively coarse resolution of the simulation, resulting in a simulation that is qualitatively correct.

A series of 30-hr full physics and sensitivity simulations, initialized at 0000 UTC 24 February 1989, were performed utilizing the MASS model (Table 1). The initial analysis started with the NCEP 2.5° resolution GOI analyses for the first-guess field and includes available NCEP rawinsonde and surface data, surface observations from moored and drifting buoys, ship reports, and weekly composite 18 km AVHRR SST data for 18–24 February 1989. A synthetic relative humidity retrieval scheme used the cloud observations and Manually Digitized Radar (MDR) data to enhance the objective rawinsonde moisture analysis. Surface observations that were spatially and temporally collocated with rawinsonde observations were used to enhance vertical profiles of relative humidity based upon the statistical correlation between observed cloud/weather categories and a statistical database of relative humidity and cloud observations for 0000 and 1200 UTC (MESO, Inc., 1995). Where Manually Digitized Radar (MDR) data indicated precipitation, the vertical moisture profile at a model grid point was enhanced via the process described in MESO, Inc. (1995).

A series of sensitivity experiments were performed to quantify the impact of latent heating, surface fluxes and grid resolution on storm intensity and track (Table 1). Hourly nudging[1] of surface wind, temperature, and moisture data as well as MDR data was successful through 0000 UTC 25 February 1989 in the full-physics *control* simulation. Horizontal grid resolution was 20 km for all experiments except the 60-km coarse simulation. A vertical resolution of 26 sigma levels was used for all simulations with the highest resolution in the lower troposphere.

4.1 Simulation results

The MASS-forecast surface low position for the control simulation agrees well with observations through the duration of the 30-hr control simulation, tracking the surface storm center northeastward along the warm side of the Gulf Stream front (Fig. 16). In contrast, the NGM forecast tracked the low northward across the Gulf Stream front into colder waters, placing the low center roughly 70 km WNW of the observed low center at 1200 UTC 24 February and approximately 180 km NNE of the observed storm position at 0000 UTC 25 February. Through 36 hours, the NGM-forecast position was more than 400 km NNE of the observed storm center (Fig. 1).

[1] See Graziano 1995 and MESO, Inc. 1995 for details regarding the methodology used in the nudging.

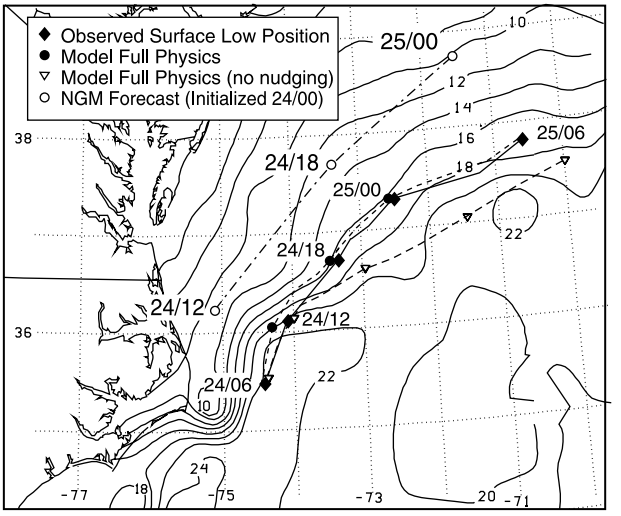

Fig. 16. Comparison of observed surface cyclone track with the forecast tracks for the NGM and MASS simulations initialized at 0000 UTC 24 February 1989; observed surface low position (solid diamonds), NGM position (circles), and positions of MASS control simulation (stars), 20-km full physics simulation without nudging (open triangles), and 60-km full physics simulation (open diamonds). The temporal resolution of the MASS and NGM forecast positions are 2 and 12 hrs, respectively (dy/hr). Thin contours are sea-surface temperature (°C) isotherms derived from composited AVHRR data for 18–24 February 1989

Analyses of MASS-forecast mean sea-level (MSL) pressure, temperature, and winds in the control simulation compare favorably with observations during the rapid development phase of the storm (compare Figs. 12 and 17). The observed and forecast position and intensity of the surface-low center and the distribution of surface winds and temperature mirror the subjective analyses. The MASS 18-hr forecast positions the storm approximately 10 km west of the observed location at 1800 UTC 24 February 1989. Consistent with observations, the simulated pressure gradient and winds increased northwest of the low. The observed and forecast positions of the warm front east of the low and trough to the southwest are nearly coincident at 1800 UTC. The model-forecast central pressure matches the observations very well through 1200 UTC, both showing a central pressure of 998 hPa (Fig. 1 inset and Fig. 18). However, the simulated storm deepened only to 996 hPa by 1800 UTC, ~6 hPa higher than analyzed. The model accurately simulated the MSL pressure over a broad region surrounding the low center but exhibited difficulty resolving the magnitude of the pressure

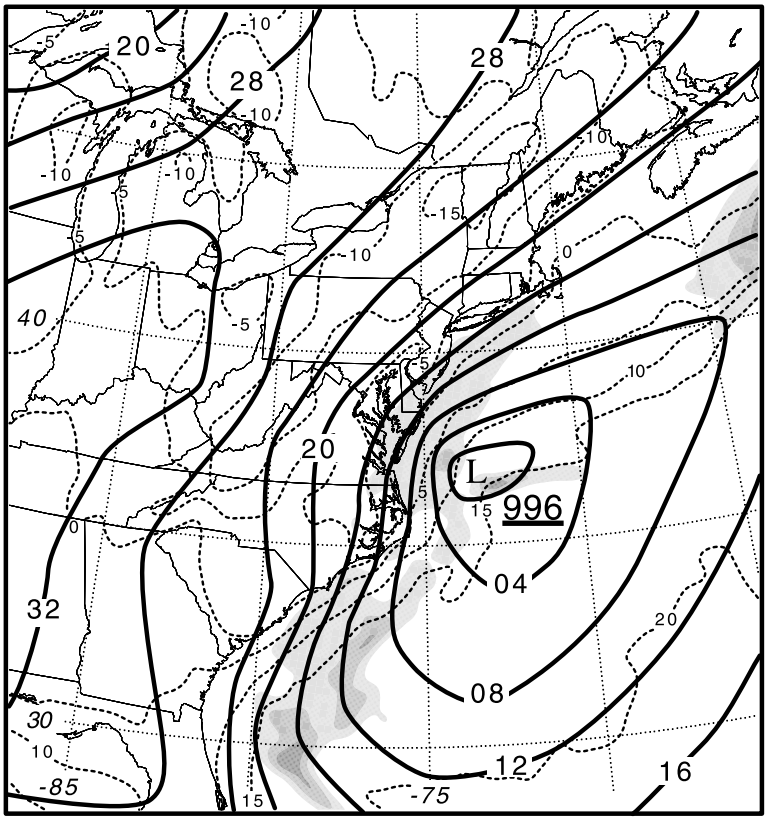

Fig. 17. Sea-level isobars (hPa, solid lines) and isotherms (°C, dashed lines) for MASS full physics control simulation for 1800 UTC 24 February 1989. Lightest shading indicates 6-hr cumulative precipitation of 10 to 20 mm, with successively darker shades representing 10-mm increments of precipitation

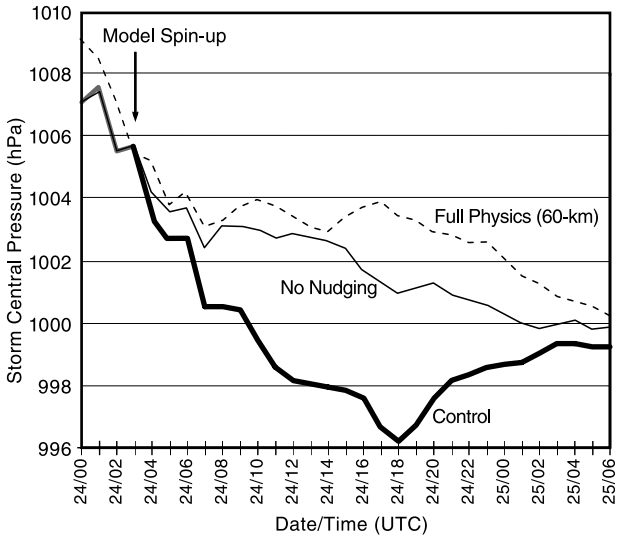

Fig. 18. Time series of storm central pressure (MSLP) for MASS control simulation (bold line), 20-km full physics simulation without nudging (thin solid), and 60-km full physics simulation (dashed)

gradient measured by aircraft in the immediate vicinity of the storm center (Fig. 12).

In the absence of upper-air data over the Gulf of Mexico and off the East Coast of the U.S., it is possible that there are errors at the upper levels in the model initial condition. However, the short wave and associated quasi-geostrophic forcing originate over land, where data coverage is adequate to document the structure. The inability of the simulation to produce a low as deep as observed is more likely the result of inadequate initialization of the meso-beta scale moisture maxima and of the relatively coarse model resolution inhibiting the development of moist and dry convection. Results from further simulations support the suggested sensitivity of the simulation to model grid resolution. As a consequence of these considerations, the question of how much of the deepening can be attributed to the action of convective latent heating versus large-scale dry dynamics cannot be quantitatively addressed in this paper. A detailed analysis of the impact of diabatic heating on simulated storm development presented in Sect. 5 will concentrate on the time period prior to 1200 UTC, when the simulated storm track and depth were most accurate.

The distance separating the control and no-nudging simulated low centers did not exceed 15 km through the 14-hr forecast valid 1400 UTC 24 February 1989 (Fig. 16). The separation between the low centers increased beyond this point to a maximum of 70 km by the 26-hr forecast valid 0200 UTC 25 February. The control simulation tracked the low farther north and generated a deeper vortex. The trend in lowest MSL pressure was similar through the first 20 hours of the simulations, although the control simulation produced a deeper cyclone beyond the 6-hr forecast (Fig. 18). The difference in lowest MSL pressure was more than 4 hPa at the time of the 18-hr forecast valid 1800 UTC 24 February, which coincides with the cessation of the observed rapid deepening phase of the cyclone.

The 60-km simulated storm location was east of the 20-km control forecast and observed positions through the duration of the simulations (Fig. 16). Additionally, the trend in the 60-km simulated lowest MSL pressure only paralleled the 20-km control simulation through the 6-hr forecast, deviating significantly thereafter (Fig. 18). In light of the significant impact nudging had on the 20-km control simulation, it is interesting to compare the performance of the 20-km full physics simulation without nudging and the 60-km full physics simulation with nudging. The latter simulation resulted in poorer forecasts of both track and intensity (Figs. 16 and 18), revealing a considerable sensitivity of the simulation to model grid resolution despite nudging.

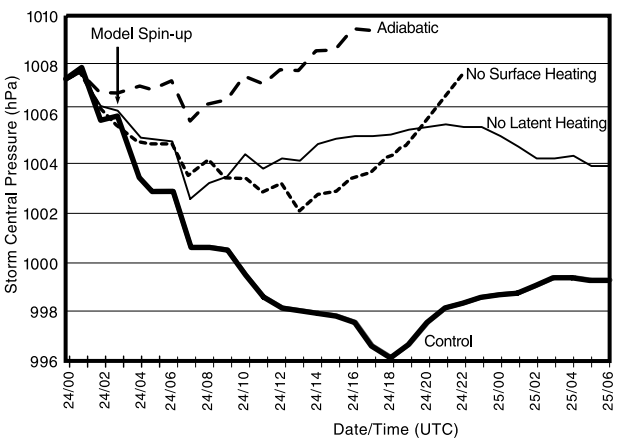

Fig. 19. Time series of storm central pressure (MSLP) for MASS control simulation (bold solid), no latent heating (thin solid), no surface heat fluxes (dashed), and adiabatic simulations (dot-dashed)

4.2 Control, no latent heating, and adiabatic simulations

The MASS storm central-pressure and track forecasts for control, no-latent heating, no-surface-heat fluxes, and adiabatic simulations are shown in Figs. 19 and 20. A notable similarity in the forecast central-pressure traces is the sharp reduction in pressure during the hour ending

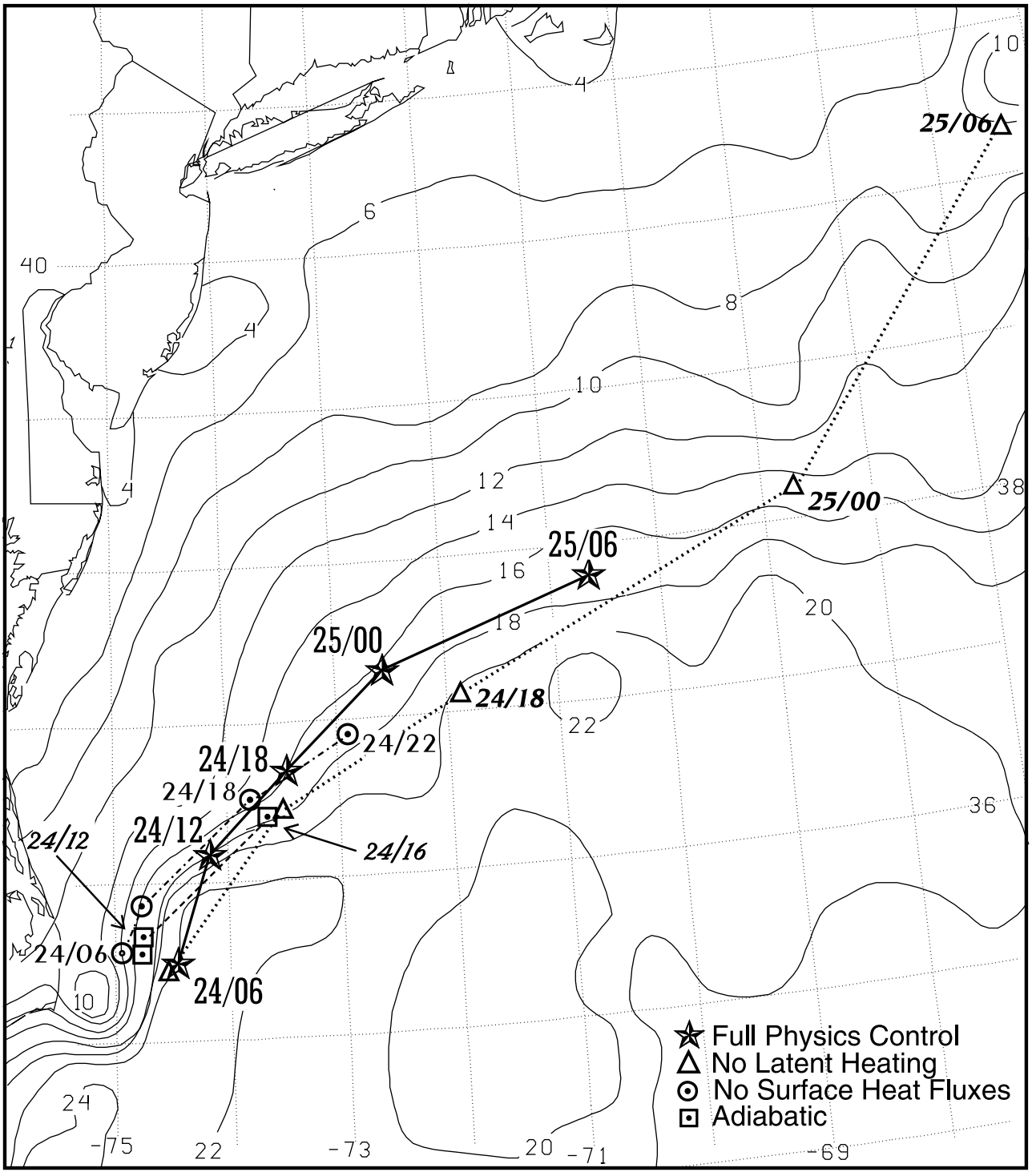

Fig. 20. As in Fig. 16 showing full physics control (stars), MASS no latent heating (open diamonds), no surface heat fluxes (open circles), and adiabatic simulations (open squares)

0700 UTC 24 February (Fig. 19). This feature is largest for the control experiment, but is also apparent in the trace for the 60-km coarse simulation (Fig. 18), suggesting that this period of deepening was, in part, the result of large scale quasi-geostrophic forcing or dry baroclinic instability.

Beyond the 7-hr forecast, the simulated MSL pressure increases in the no-latent heating and adiabatic simulations. The adiabatic simulation yielded the weakest and shortest lived vortex, underscoring the importance of diabatic processes on the development and evolution of this cyclone. In contrast, the simulated storm central pressure in the no-surface-heat-fluxes simulation continues to decrease from 0800 to 1100 UTC and from 1200 to 1300 UTC on 24 February (Fig. 19). In spite of the absence of surface-heat fluxes, latent heating associated with available moisture in the air serves to destabilize the atmosphere in areas of grid and sub-grid scale precipitation in proximity to the storm center and results in modest surface pressure falls.

The surface vortex in the no-latent-heating simulation tracked considerably east and north of the control vortex. In fact, the 18- and 24-hr forecasts for the no-latent-heating simulation placed the surface cyclone approximately 170 km ENE and 320 km ENE of the control experiment forecast position, respectively (Fig. 20). Hence, the absence of condensational warming yielded a weaker and more rapidly propagating vortex with a more easterly track. The positions of the surface cyclone for the no-surface-heat-fluxes and adiabatic simulations are not plotted after the 22- and 16-hr forecasts, respectively, since no discernible vortex (closed isobar) was evident beyond these times (Fig. 20). While a vortex was discernible, however, the forecast tracks were generally west of the control simulation.

5. Diabatically driven ageostrophic circulations and cyclone development

The use of potential-vorticity diagnostics has become popular recently in diagnosing cyclogenesis. However, in this section we present an alternative approach to shed light on the mechanism underlying the mesoscale cold-air cyclogenesis. The relationship between the convection and the mesoscale mass and momentum adjustments during the cold-air cyclogenesis are investigated via the following quantities: (i) the integrated mass divergence, (ii) the isallobaric component of the ageostrophic wind [$V_{isall} = -f_o^{-2}\nabla(\partial\phi/\partial t)$], and (iii) the Lagrangian Rossby number [$R_o = (DV/Dt)/(fV)$].

Motivation for this approach comes from the scale of the cold-air cyclogenesis. Observational evidence suggests that the wavelength of the cyclonic circulation is smaller than the Rossby radius of deformation ($L_R = NH/f$, where N is the Brunt-Väisälä frequency, H the scale height of the disturbance, and f the Coriolis parameter). For example, at 0600 UTC 24 February, at the onset of the period of rapid development just east of the North Carolina coast, the Hatteras sounding gives observed values of $N \sim 0.0120\,s^{-1}$, $H \sim 7663$ m, and $f \sim 8.37 \times 10^{-5}\,s^{-1}$. This produces an observed value of $L_R \sim 1100$ km, nearly twice the ~600 km wavelength of the observed pressure fall and area of cyclonic circulation. Using aircraft data for 2000 UTC on 24 February, N is $\sim 0.0124\,s^{-1}$, $H \sim 7864$ m, and $f \sim 8.78 \times 10^{-5}\,s^{-1}$, resulting in an observed value of $L_R \sim 1110$ km, consistent with the earlier value.

During the rapid development phase of the cold-air cyclogenesis, three periods of enhanced surface pressure reduction occurred, 0600–0700 UTC, 0900–1100 UTC, and 1600–1800 UTC 24 February (Fig. 19). These three time periods correspond to periods of enhanced convective latent heat release in the control simulation.[2] In light of the influence of quasi-geostrophic forcing on all simulations from 0600–0700 UTC and better performance of the control simulation prior to 1200 UTC, the mesoscale impact of diabatic processes on cyclogenesis is investigated during the 2-hour period ending 1100 UTC 24 February. To focus on the impact of the convective latent-heat release on the cyclogenesis and because of the similarities between the results of the various sensitivity runs, only the results of the no-latent-heat and control runs are explicitly compared here.[2]

At 1000 UTC 24 February the surface vortex in the control simulation (Fig. 21a) is considerably stronger than the vortex in the no-latent-heating (Fig. 22a). Elevated surface relative vorticity

[2] The reader is referred to Graziano (1995) for additional analysis.

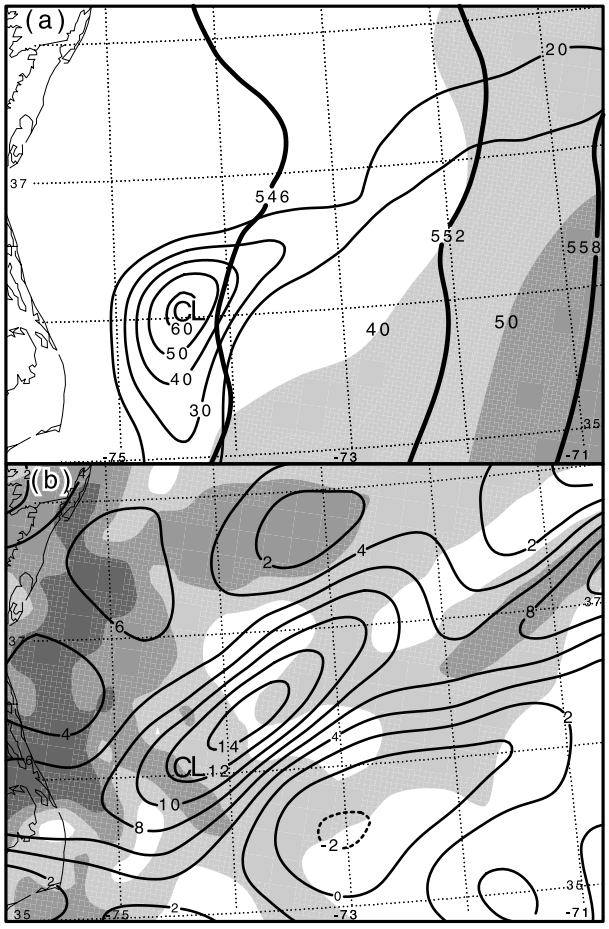

Fig. 21. MASS full physics analyses valid 1000 UTC 24 February 1989. The location of surface relative vorticity maxima is shown by C, and the location of surface low pressure center is shown by L; (**a**) 500-hPa height contours (dam, heavy solid lines), and isotachs shaded $>40\,\mathrm{m\,s^{-1}}$). MSL relative vorticity ($\geq 20 \times 10^{-5}\,\mathrm{s^{-1}}$, thin solid line); (**b**) 500-hPa Lagrangian Rossby number (shaded ≥ 0.5 at 0.5 increments), and 975–150-hPa layer integrated horizontal mass flux ($\times 10^{-3}\,\mathrm{mb\,s^{-1}}$, thin solid line)

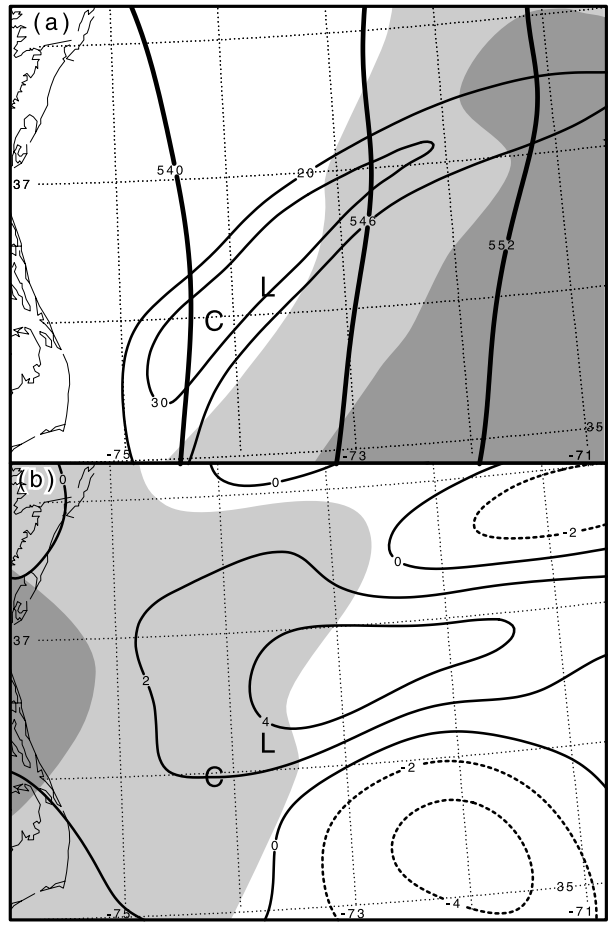

Fig. 22. As in Fig. 21, but for MASS no-latent-heating simulation

extending northeast of the surface low coincides with the position of the warm front (Fig. 21a). A broad region of convective precipitation, occurring along and poleward of this front encompasses the surface cyclone in the control simulation (Fig. 23a). In the area of condensational heating in the vicinity of the control surface cyclone, the 500-hPa heights rise and are $\sim$60 m greater than their counterparts in the no-latent-heating run (Figs. 21a and 22a). This suggests that latent-heat release is predominantly responsible for the height (mass) perturbation. In response to the 500-hPa height rises, in the presence of baroclinicity, the isallobaric component of the ageostrophic wind ($V_{isall} = -f_o^{-2}\nabla(\partial f/\partial t)$) is large and divergent above and immediately downstream of the surface low (Fig. 23a). The isallobaric divergence aloft hydrostatically results in lower pressure at sea level in the control simulation ($\sim$6 hPa lower than the no-latent-heating simulation at 1100 UTC in Fig. 19). Subsequent enhanced convergence at low levels generates vorticity through frictional production and conservation of angular momentum. As a result, the surface circulation is stronger ($\zeta_{max} > 60 \times 10^{-5}\,\mathrm{s^{-1}}$) in the control simulation. The scale of these signatures is consistent with the scale of the latent heating (Figs. 21 and 23) and consistent with Gall (1976). In contrast, the central pressure associated with the surface cyclones in the no-latent-heating simulation has risen, and 500-hPa geopotential heights have decreased significantly in the region of cyclonic

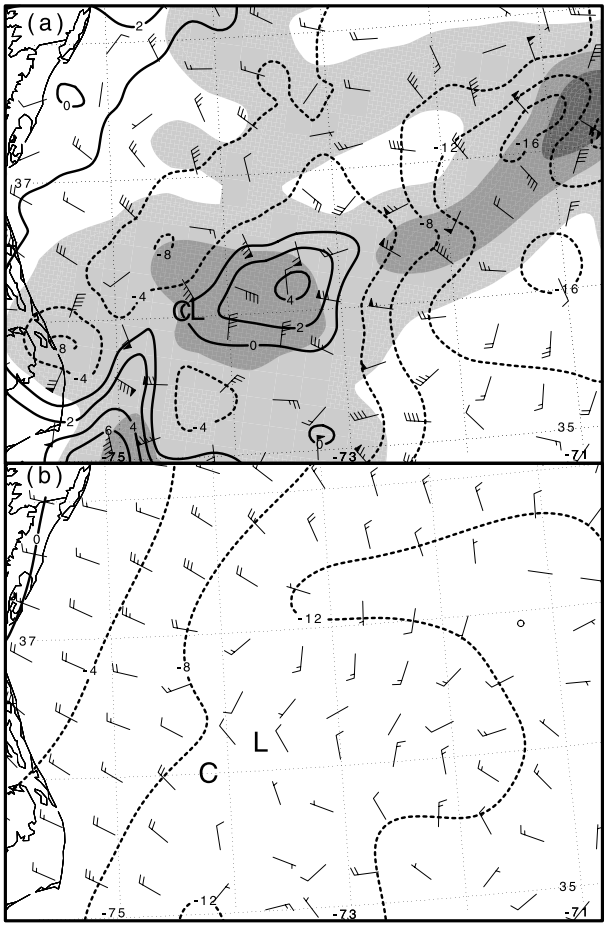

Fig. 23. 500-hPa isallobaric ageostrophic wind (plotted in standard convention), 1-hr geopotential height change (m, solid/dashed line), and cumulative convective precipitation (shaded $\geq$.25 mm at increments of 2.5 mm) for the 1-hr period ending 1000 UTC 24 February. The location of surface relative-vorticity maxima is shown by C, and the location of the surface low pressure center is shown by L; (**a**) full physics (control) simulation; (**b**) no-latent-heating simulation

flow aloft from that seen in the previous hour (not shown). This indicates that the combined effects of low-level warm advection and surface sensible heating, in the absence of latent heating, are not sufficient to cause ridging over the surface cyclone in the mid to upper troposphere.

Large values of the Lagrangian Rossby number ($R_o > 0.5$) at 500 hPa in the control simulation indicate a large time-rate-of-change in the flow aloft over the surface low center and reflect the mesoscale momentum adjustment to the mass perturbation (Fig. 21b). In contrast, values of the Lagrangian Rossby number are considerably smaller in the no-latent heating run (Fig. 22b). A direct manifestation of the large Lagrangian Rossby number values is the marked difference in layer-integrated mass flux divergence between the full physics and sensitivity simulations. At 1000 UTC in the control simulation, values of 975-150-hPa layer-integrated mass flux in the immediate vicinity of the surface low are more than three times larger than comparative values in the no-latent-heating simulation (Figs. 21b and 22b), suggesting that latent heating (moist convection) is a key ingredient in generating the larger values of integrated mass flux in the column of air above the control cyclone. This result is consistent with the findings of Kaplan and

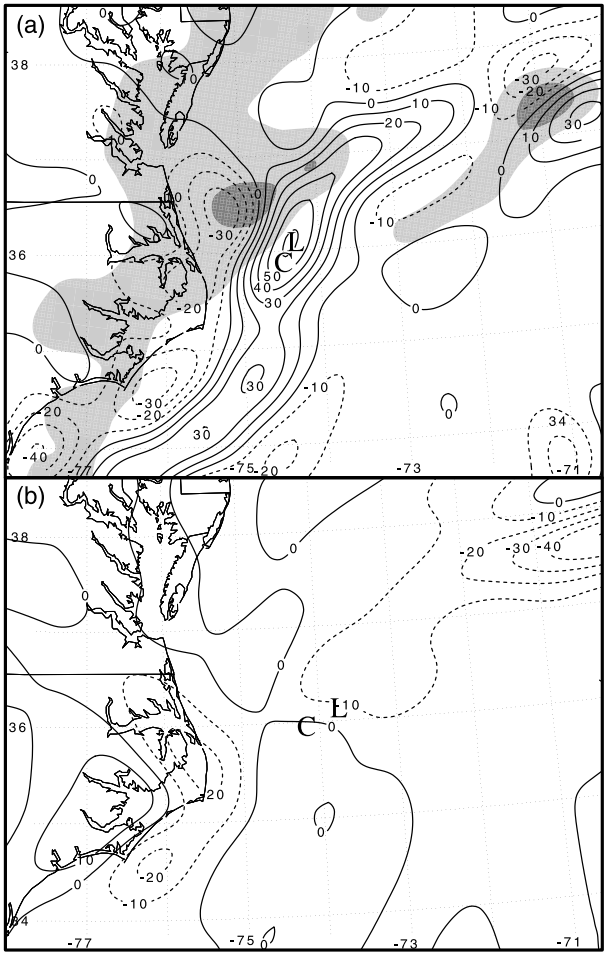

Fig. 24. MASS simulations valid 0900 UTC 24 February 1989. The position of the surface low pressure center is given by L. Tilting term (solid and dashed contours $\times 10^{-9}\ s^{-1}$), and cumulative convective precipitation (shaded $\geq$2.5 mm at increments of 2.5 mm) for the 1-hr period ending 0900 UTC 24 February; (**a**) For MASS control simulation; (**b**) For MASS no-latent-heating simulation

Businger (1994). Surface pressure falls and isallobaric winds are correspondingly larger (Figs. 19 and 23).

During the 12-hr period of rapid deepening ending at 1800 UTC 24 February 1989, the intensity and depth of the lower tropospheric vortex are consistently greatest in the full physics simulation. Contributions to the local vorticity tendency include horizontal advection, vertical advection, stretching, and tilting (Holton, 1992). The relative contribution of these four terms to the local vorticity tendency was similar for all simulations through the 12-hour period with one notable exception, the tilting term. The tilting term was consistently a source of vorticity above and immediately downstream of the surface vortex in the full physics simulation (Graziano, 1995). In contrast, it served as a recurring sink of vorticity above and in the forward path of the lower tropospheric vortices in the no-latent-heating run, suggesting that latent heating was responsible for the observed discrepancy. As an example, Eulerian vorticity analyses for 0900 UTC 24 February show that the tilting term generates vorticity at low levels over and downstream of the surface low in the control simulation (Fig. 24a). In contrast, the tilting term was small in the no-latent-heating simulation, providing a negative contribution to the vorticity tendency over and downstream of the surface low (Fig. 24b).

6. Conclusions and discussion

This paper documents the structure and evolution of a cold-air cyclone that produced moderate to heavy snowfall along the mid-Atlantic coast of the U.S. on 24–25 February 1989. The storm is noteworthy for its low-latitude formation within a polar air mass and the attendant mesoscale core and frontal structures. Moreover, the impact of surface fluxes over the Gulf Stream on the evolution and track of the storm presented significant challenges to operational NWP models and forecasters. NOAA P-3 research aircraft observations, satellite imagery, drifting buoy, and operational surface and upper air data collected during the ERICA field program were used to construct synoptic and mesoscale analyses of this cyclone. Simulations of the storm were produced by the Mesoscale Atmospheric Simulation System (MASS) model to investigate the relationship between convective latent-heat release surrounding the surface low center, enhanced divergence aloft, and the track of the cold-air cyclone. Mesoscale processes and instability mechanisms responsible for the rapid development of the cyclone were examined via a series of modeling sensitivity experiments where latent heating and surface energy fluxes are alternately turned off and on and model resolution was varied.

6.1 Principal conclusions

(1) Differential surface fluxes in the vicinity of the Gulf Stream led to the formation of a well-defined baroclinic zone at low levels. The baroclinic zone strengthened and assumed the characteristics of a shallow warm front that extended northeastward from the low center as the cyclone matured. Enhanced cyclonic vorticity, moisture flux convergence, clouds, and precipitation accompanied the front.

(2) A series of shallow thermally forced vortices of small wavelength ($\sim$200 km) formed along the baroclinic zone in the area of maximum surface-heat fluxes offshore the Carolinas.

(3) Baroclinic instability associated with a vigorous short-wave trough aloft led to destabilization of the tropospheric lapse rate through differential thermal advection and large scale lifting. Consequently, the outbreak of deep convection off the North Carolina coast coincided with rapid intensification of the northernmost vortex.

(4) The mature cold-air cyclone included a mesoscale core of low pressure characterized by a cloud-free center surrounded by spiral bands of deep convection and enhanced winds.

(5) The observed track of the low followed the axis of the warm front, which in turn followed the axis of maximum SST gradient associated with the Gulf-Stream front. Accurate simulation of the storm track required high-resolution SST data in the initial condition and a high-resolution full-physics (control) run that included moisture nudging during the early hours of the simulation.

(6) The MASS model in the control simulation was able to accurately reproduce observed patterns of MSL pressure, temperature gradients, and winds during the rapid development phase of the storm. Although the simulated track agrees very well with observations, the model under forecast central pressure of the storm's deepest stage.
(7) Sensitivity experiments show that latent heating in deep convection associated with the incipient surface low produced a mesoscale height perturbation aloft. The resulting acceleration of the flow aloft substantially increased the integrated mass divergence above the surface cyclone, fostering enhanced deepening on the scale observed.
(8) Numerical experiments show that latent heating associated with sustained moist convection near the surface-low center generated vorticity at low levels via tilting.

6.2 Discussion

Cyclogenesis occurred along a shallow baroclinic zone oriented southwest to northeast, created by differential diabatic heating and shear and confluent deformation along the northern wall of the Gulf Stream. The surface low formed over the general area where the Gulf Stream comes within 70 km of the North Carolina coast. At the outset of rapid deepening, surface heat fluxes were calculated to be $\sim$1000 W m^{-2} into air ingested by the storm, and an upper-level shortwave trough approached the Carolina coast. When cold advection aloft and upward quasi-geostrophic forcing crossed the coast, thunderstorms were triggered in the preconditioned, unstable vicinity of the surface-low center, and rapid cyclogenesis ensued. These circumstances are not dissimilar to those observed in midlatitude cyclones along the U.S. East Coast, in which a rapid deepening phase comprises only a small fraction of the total time elapsed during the cyclogenetic event (Sanders and Gyakum, 1980; Bosart, 1981; Roebber, 1984; Uccellini et al, 1987; Gyakum and Barker, 1988; Kocin and Uccellini, 1990).

Nevertheless, the mesoscale structures associated with the cold-air cyclogenesis and their evolution are distinct. As cyclogenesis progressed, the geography of the U.S. East Coast and Gulf Stream in large measure governed the development of the warm frontal structure. The contrasting histories of surface fluxes in the air streams on the northeast and southwest sides of the shear line contribute overwhelmingly to the formation of the shallow but well-defined baroclinic zone. In the cold westerly flow off the Carolina coast, significant diabatic heating was observed over the warm Gulf Stream. Evidence of the air-mass modification is reflected in the surface temperature analyses and in the evolution of the clouds in the satellite imagery from clear air to cloud streets and open cell convection as the air moves offshore. In contrast, air approaching from the northeast tended to have shorter trajectories over much colder water and experienced significantly less modification from surface fluxes.

The evolution of a strong warm front and the relative absence of cold frontogenesis in the mature cold-air cyclone are in sharp contrast to previous literature describing the frontal evolution in cyclones forming in polar air over the eastern Atlantic and Pacific (Anderson et al, 1969; Reed, 1979; Carleton, 1985; Mullen, 1983; Browning and Hill, 1984). Thermal advection patterns characteristic of cold fronts have been documented in a number of landfalling polar lows along the west coast of the U.S. (Locatelli et al, 1982; Reed and Blier, 1986; Businger and Hobbs, 1987; Businger and Walter, 1988). These circulations are associated with generally north–south oriented troughs that mark the leading edge of cold advection over the Pacific Ocean. In these cases, warm fronts were notably absent. In cases of close proximity between polar lows and wave cyclones a number of interactions have been documented in the literature (e.g., Businger and Reed, 1989). Instant occlusion is a term used to describe a relatively common interaction in which frontogenesis associated with the polar low provides the occluded front and the frontal wave provides the warm and cold fronts to the storm. After the instant occlusion these storms appear identical to classical occluded systems in the cloud signatures seen in satellite imagery. McGinnigle et al (1988) analyzed several cases of instant occlusions over the north Atlantic using synoptic and mesoscale data and numerical model diagnostics. They suggest an alternative analysis scheme to the traditional instant

occlusion in which the occlusion is replaced by a warm front, and the secondary cold front associated with the polar trough becomes the more significant cold-air boundary. This model appears more applicable in the present case with respect to the warm frontal structure; however, the cold air boundary remained relatively unfocused in the analyses presented here because of significant modification of the cold air by enhanced surface fluxes to the south of the low.

One of the distinctive aspects of this case study is the compact scale of the mature cold-air cyclone. During the period of rapid development, between 0600 UTC and 1800 UTC 24 February, the mean wavelength of the cyclonic circulation is <600 km. This subsynoptic scale cyclone is approximately twice the length scale of the region of enhanced convection with which its development is closely coupled, an observation reminiscent of polar-low phenomena (e.g., Rasmussen, 1981; 1985; Businger and Baik, 1991).

During its mature phase on 25 February, the cyclone central pressure remained near 990 hPa, and then deepened an additional 4 mb after 0600 UTC, despite little apparent quasi-geostrophic forcing. Strong surface winds ($>30\,\mathrm{m\,s^{-1}}$) and enhanced surface fluxes ($>1200\,\mathrm{W\,m^{-2}}$) were observed in immediate proximity of the low center as it continued to track along the northern wall of the Gulf Stream. Analyses of ERICA flight level, satellite, and radar data during this stage reveal a warm inner core, with a sharp pressure gradient near the center, and a quasi-symmetric structure of convective clouds surrounding a clear center. These observations are reminiscent of observations and model results for polar lows at higher latitudes (e.g., Shapiro et al, 1987; Økland and Schyberg, 1987; Businger and Baik, 1991). Similar characteristics have also been documented in the warm seclusion region of explosive marine cyclones (Neiman and Shapiro, 1993; Neiman et al, 1993).

Numerical and observational evidence for a link between convection and mesoscale cyclogenesis and the storm's track along the axis of maximum potential thickness anomaly support the suggestion that a combination of surface fluxes and latent heating are instrumental in maintaining the low during its mature stage (Emanuel, 1983b; Emanuel and Rotunno, 1989; Albright et al, 1995).

Numerical sensitivity studies of the ERICA cold-air cyclone were undertaken using the MASS model to investigate the non-linear response of the mass field to the convection. The numerical results were not conclusive regarding the magnitude of the deepening that can be attributed to the diabatic affects versus dynamical forcing. Rather, the primary contribution of the numerical modeling component of the paper is the introduction of a novel approach, based on the balance equation, to analyze the mechanics behind the impact of latent heat release on cyclone deepening. The focus of this analysis is on a period during which the simulation did accurately reproduce the intensity and location of the low. The results of the analysis show that convective latent-heat release produced a mesoscale perturbation of the flow aloft that contributed to enhanced divergence over the developing low center. The results for the control simulation show that the scale of enhanced upper-level divergence and the scale of the resulting cyclogenesis are linked to the area of convective precipitation. Moreover, latent heating associated with sustained moist convection near the surface low center generated vorticity at low levels via tilting.

Satellite imagery and aircraft data support the observation that the warm front was an axis of moisture-flux convergence that fed modified unstable air toward the developing surface low at low levels. The observed track of the low followed the axis of the warm front, which in turn followed the axis of maximum SST gradient associated with the Gulf-Stream front (Fig. 1). A similar link between the track of the model cyclone and the role played by the Gulf Stream in the evolution of the convection is indicated by the simulation results. In order to produce an accurate track forecast, a high-resolution run of the MASS model had to include both a high-resolution SST analysis in the initial condition and moisture nudging during the early hours of the simulation.

The numerical studies confirm the role of latent heating and surface fluxes in the initial cyclogenesis and their impact on the storm track. However, it is important to emphasize the fact that the convection in this case is occurring in the context of a baroclinic environment provided by a vigorous short-wave trough aloft, without

which the convection would have remained shallow and the resulting weak low may have tracked well to the north over colder water as was forecast by the NGM.

Ultimately, the control simulation under-forecast the storm central pressure by ~6 hPa at the end of the rapid deepening phase and failed to maintain the strength of the low on 25 February. The sensitivity of the model results to resolution suggests that increasing model resolution and including a non-hydrostatic implementation with a buoyancy-based convective parameterization and/or explicit cloud physics with sufficient resolution (~1 km grid) may overcome these shortcomings. These suggestions are currently being pursued in ongoing investigations.

It is hoped that the unique characteristics of the cold-air cyclone documented in this paper and the conclusions drawn from the numerical sensitivity studies will generate interest and will have application for improved operational forecasting of future events of this nature.

Appendix

The bulk aerodynamic relationship employed in the calculation of the sensible (Q_H) heat flux is written

$$Q_H = \rho C_p (\overline{w'\theta'})_s \approx \rho C_p C_H \bar{M}_{10} (\bar{\theta} - \bar{\theta}_G),$$

where ρ = air density, Cp = specific heat at constant pressure, C_H = bulk transfer coefficient, $\bar{M}_{10}$ = mean wind speed at 10 m, and $\bar{\theta} - \bar{\theta}_G$ = the air–sea temperature difference. C_H was approximated by combining Charnock's (1955) relationship: $z_0 = 0.015\, u^{*2}/g$, with the log wind profile under neutral conditions,

$$\bar{M} = \frac{u_*}{k} \ln \left[\frac{z}{z_0} \right],$$

in accordance with G.I. Taylor's (1916) velocity squared law

$$C_D = \left[\frac{u_*^2}{\bar{M}^2} \right],$$

to yield $C_{DN} = 4.4 \times 10^{-4}\, \bar{M}_{10}^{0.55}$ (Stull, 1993). $\bar{M}_{10}$ was computed via a four-step process. First, subjective mean sea-level (MSL) pressure (and temperature) analyses were constructed and gridded at $1^\circ \times 1^\circ$ spacing. Second, surface observations from moored and drifting buoys, ships, and standard surface reporting stations were gridded at $1^\circ \times 1^\circ$ using a Barnes (1973) analysis with the gridded subjective sea level analyses serving as a first guess field. Third, the geostrophic wind was calculated from the gridded MSL pressure. Fourth, the surface wind was estimated using a linear relationship (for neutral conditions) proposed by Hasse and Wagner (1971) where $\bar{M}_{10} = (0.56\, \mathrm{U_g} + 2.4\, \mathrm{m\, s^{-1}})$.

A good correlation between calculated $\bar{M}_{10}$ values and available ship wind reports gives credibility to this technique. The latent heat flux (Q_E) was calculated using a similar expression

$$Q_E = \rho L_v (\overline{w'q'})_s \approx \rho L_v C_E \bar{M}_{10} (\bar{q} - \bar{q}_G),$$

where L_v = the latent heat of evaporation at 20 °C, $C_E = C_H$ as defined above, $\bar{q}$ = mixing ratio at the 10-m level, and $\bar{q}_G$ = the mixing ratio at the ocean surface. GOI data was gridded at $1^\circ \times 1^\circ$ using two passes with a Barnes (1973) analysis, and the lapse of dew point between the 1000 hPa and 925 hPa levels was utilized to extrapolate the 1000 hPa dew point to the 10-m level. The estimated values of surface dew point temperature agreed well with available surface dew point observations. Mixing ratios at the ocean surface and 10-m level were computed from the dew point temperatures, and latent heat fluxes were calculated on a $1^\circ \times 1^\circ$ lat./lon. grid at 1200 UTC 24 and 0000 UTC 25 February. The sea-surface temperatures used in these calculations were a gridded 1° resolution weekly composite of Advanced Very High-resolution Radiometer (AVHRR) data for 16–22 February 1989.

Acknowledgments

Special thanks are extended to Steve Chiswell, Bill Bauman, and Michael Adams for their technical support and collaboration. We would like to thank Owen Hertzman for providing aircraft radar data. The manuscript benefited from constructive comments from Allen Riordan, Sethu Raman, Gerald Watson, and two anonymous reviewers. This research is supported by the National Science Foundation under grant ATM-99-09011. School of Ocean and Earth Science and Technology contribution no. 6299.

References

Albright MD, Reed RJ, Ovens DW (1995) Origin and structure of a numerically simulated polar low over Hudson Bay. Tellus 47A: 834–848

Anderson RK, Ashman JP, Bittner F, Farr GR, Ferguson EW, Oliver VJ, Smith AH (1969) Application of meteorological satellite data in analysis and forecasting. ESSA Tech. Rep. NESC51, Government Printing Office, Washington, DC [NTIS AD-697033]

Arya PSP (1988) Introduction to micrometeorology; Chicago, IL: Academic Press, 307 pp

Barnes SL (1973) Mesoscale objective analysis using weighted time-series observations. NOAA Tech. Memo. ERL NSSL-62, Norman, OK, 60 pp

Bergeron T (1928) Über die dreidimensional verknüpfende Wetteranalyse I. Geofys Publ 5(6): 111 pp

Bosart LF (1981) The president's day snowstorm of 18–19 February 1979: A subsynoptic-scale event. Mon Wea Rev 109: 1542–1566

Browning KA, Hill FF (1984) Structure and evolution of a mesoscale convective system near the British Isles. Quart J Roy Met Soc 110: 897–913

Businger S (1985) The synoptic climatology of polar low outbreaks. Tellus 37: 419–432

Businger S, Baik JJ (1991) An arctic hurricane over the Bering Sea. Mon Wea Rev 119: 2293–2322

Businger S, Hobbs PV (1987) Mesoscale and synoptic scale structure of two comma cloud systems over the Pacific Ocean. Mon Wea Rev 115: 1909–1928

Businger S, Reed RJ (1989) Cyclogenesis in Cold Air. Wea Forecast 2: 110–133

Businger S, Walter B (1988) Comma cloud development and associated rapid cyclogenesis over the Gulf of Alaska: A case study using aircraft and operational data. Mon Wea Rev 116: 1103–1123

Carleton AM (1985) Satellite climatological aspects of the ''polar low'' and ''instant occlusion.'' Tellus 37: 433–450

Charnock H (1955) Wind stress on a water surface. Quart J Roy Meteor Soc 81: 639–640

Cram JM, Kaplan ML, Mattocks CA, Zack JW (1991) The use and analysis of profiler winds to derive mesoscale height and temperature fields: Simulation and real-data experiments. Mon Wea Rev 119: 1040–1056

Davis CA, Emanuel KA (1988) Observational evidence for the influence of surface heat fluxes on rapid maritime cyclogenesis. Mon Wea Rev 116: 2649–2659

desJardins ML, Brill KF, Jacobs S, Schotz SS, Bruehl P (1992) GEMPAK5 Users Manual Version 5.1, NASA/GSFC, National Meteorological Center, and Unidata Program Center/UCAR, 267 pp

Doyle JD, Warner TT (1993) Nonhydrostatic simulation of coastal mesobeta scale vortices and frontogenesis. Mon Wea Rev 121: 3371–3392

Emanuel KA (1983a) The lagrangian parcel dynamics of moist-symmetric instability. J Atmos Sci 40: 2368–2376

Emanuel KA (1983b) On assessing local conditional symmetric instability from atmospheric soundings. Mon Wea Rev 111: 2016–2033

Emanuel KA, Rotunno R (1989) Polar lows as arctic hurricanes. Tellus 41A: 1–17

Farrell BF (1984) Modal and nonmodal baroclinic waves. J Atmos Sci 41: 668–673

Gall R (1976) The effects of released latent heat in growing baroclinic waves. J Atmos Sci 33: 1686–1701

Gigi A (1989) The New York City Snowstorm That Never Was. NWS Eastern Region Technical Attachment No 89-14, 4 pp

Graziano T (1995) Analysis and numerical modeling of convectively driven ageostrophic circulations and their role in the rapid cold-air cyclogenesis during ERICA IOP8. Ph.D. Thesis, MEAS, North Carolina State University, Raleigh, NC, 76795, 201 pp

Grossman RL, Betts AK (1990) Air-Sea Interaction During An Extreme cold Air Outbreak From The Eastern United States. Mon Wea Rev 118(2): 324–342

Gyakum JR, Barker ES (1988) A case study of explosive subsynoptic-scale cyclogenesis. Mon Wea Rev 116: 2225–2253

Hadlock R, Krietzberg CW (1988) The Experiment on Rapidly Intensifying Cyclones over the Atlantic (ERICA) field study: Objectives and plans. Bull Am Meteor Soc 69: 1309–1320

Hasse L, Wagner V (1971) On the relationship between geostrophic and surface wind at sea. Mon Wea Rev 99: 255–260

Holton JR (1992) An introduction to dynamic meteorology. San Diego, CA: Academic Press, 511 pp

Huang CY, Raman S (1991) Numerical simulation of January 28 cold air outbreak during GALE. Part II: The mesoscale circulation and marine boundary layer. Bound-Layer Meteor 56: 51–81

Huang CY (1992) A three dimensional numerical investigation of a Carolina coastal front and the Gulf Stream rainband. J Atmos Sci 49: 560–584

Kaplan ML, Businger S (1994) A paradigm linking unbalanced ageostrophic adjustments to the explosive development phase in extratropical cyclones. In the Life Cycles of Extratropical Cyclones: Volume III, Bergen, Norway 388 pp

Kaplan ML, Karyampudi VM (1992) Meso-beta scale numerical simulations of terrain drag-induced alongstream circulations. Part I: Midtropospheric frontogenesis. Meteor Atmos Phys 49: 133–156

Kaplan ML, Zack JW, Wong VC, Tuccillo JJ (1982) Initial results from a Mesoscale Atmospheric Simulation System and comparisons with the AVE-SESAME I data set. Mon Wea Rev 110: 1564–1590

Koch SE (1985) Ability of a regional scale model to predict the genesis of intense mesoscale convective systems. Mon Wea Rev 113: 1693–1713

Koch SE, Skillman WC, Kocin PJ, Wetzel PJ, Brill KF, Keyser DA, McCumber MC (1985) Synoptic-scale forecast skill and systematic errors in the MASS 2.0 numerical model. Mon Wea Rev 113: 1714–1737

Kocin PJ, Uccellini LW, Zack JW, Kaplan ML (1985) A mesoscale numerical forecast of an intense convective snowburst along the East Coast. Bull Amer Meteor Soc 66: 1412–1424

Kocin PJ, Uccellini LW (1990) Snowstorms along the Northeastern Coast of the United States: 1955 to 1985. Meteor Monogr 44: 280 pp

Lin Y-L (1989) Inertial and frictional effects on stratified flow past an isolated heat source. J Atmos Sci 46: 921–936

Lin Y-L (1990) A theory of cyclogenesis forced by diabatic heating. Part II: A semigeostrophic approach. J Atmos Sci 47: 1755–1777

Locatelli JD, Hobbs PV, Werth JA (1982) Mesoscale structures of vortices in polar air streams. Mon Wea Rev 110: 1417–1433

McGinnigle JB, Young MV, Bader MJ (1988) The development of instant occlusions in the North Atlantic. Meteor Mag 117: 325–341

Manobianco JL, Koch SE, Karyampudi VM, Negri AJ (1994) The impact of assimilating satellite derived precipitation rates on numerical simulations of the ERICA IOP4 cyclone. Mon Wea Rev 122: 341–365

MESO Inc (1995) MASS Version 5.8 Reference Manual, MESO, Inc., Troy, New York, 120 pp

Mullen SL (1983) Explosive cyclogenesis associated with cyclones in polar air streams. Mon Wea Rev 111: 1537–1553

National Oceanic and Atmospheric Administration (1985) NMC models and automated operations, Technical Publication Bulletin #355

Neiman PJ, Shapiro MA (1993) Frontal cyclone evolution and thermodynamic air sea interaction. Mon Wea Rev 121: 2153–2176

Neiman PJ, Shapiro MA, Fedor LS (1993) The life cycle of an extratropical marine cyclone. Part II: Mesoscale structure and diagnostics. Mon Wea Rev 121: 2177–2199

Økland H, Schyberg H (1987) On the contrasting influence of organized moist convection and surface heat flux on a barotropic vortex. Tellus 39A: 385–389

Petterssen S, Smebye SJ (1971) On the development of extra-tropical cyclones. Quart J Meteor Soc 97: 457–482

Rasmussen E (1981) An investigation of a polar low with a spiral cloud structure. J Atmos Sci 38: 1785–1792

Rasmussen E (1985) A case study of polar low development over the Barents Sea. Tellus 37A: 407–418

Reed RJ (1979) Cyclogenesis in polar airstreams. Mon Wea Rev 107: 38–52

Reed RJ, Blier W (1986) A case study of comma cloud development in the Eastern Pacific. Mon Wea Rev 114: 1681–1695

Reed RJ, Danielsen EF (1959) Fronts in the vicinity of the tropopause. Arch Meteor Geophys Bioklim A11: 1–17

Roebber PJ (1984) Statistical analysis and updated climatology of explosive cyclones. Mon Wea Rev 112: 1577–1589

Rosenblum HS, Sanders F (1974) Mesoanalysis of a coastal snowstorm in New England. Mon Wea Rev 102: 433–442

Sanders F, Bosart LF (1985) Mesoscale structure in the megalopolitan snowstorm of 11–12 February 1983. Part I: Frontogenetical forcing and symmetric instability. J Atmos Sci 42: 1050–1061

Sanders F, Gyakum JR (1980) Synoptic-dynamic climatology of the ''bomb.'' Mon Wea Rev 108: 1589–1606

SethuRaman S, Riordan AJ, Holt T, Stunder M, Hinman J (1986) Observations of the marine boundary layer thermal structure over the Gulf Stream during a cold air outbreak. J Clim Appl Meteor 25: 14–21

Shapiro MA, Fedor LS, Hampel T (1987) Research aircraft measurements of a polar low over the Norwegian Sea. Tellus 37A: 272–307

Stull RB (1993) An introduction to boundary layer meteorology. Norwell, MA: Kluwer Academic Publishers, 666 pp

Taylor GI (1916) Conditions at the surface of a hot body exposed to the wind. Brit Adv Com Aero Rep Memor 272

Uccellini LW, Petersen RA, Brill KF, Kocin PJ, Tuccillo JJ (1987) Synergistic interactions between an upper-level jet streak and diabatic processes that influence the development of a low-level jet and a secondary coastal cyclone. Mon Wea Rev 115: 2227–2261

Warner TT, Lakhatakia MN, Doyle JD, Pearson RA (1990) Marine atmospheric boundary layer circulations forced by Gulf Stream sea-surface temperature gradients. Mon Wea Rev 118: 309–323

Wayland RJ, Raman S (1989) Mean and turbulent structure of a baroclinic marine boundary layer during the 28 January 1986 cold air outbreak (GALE 86). Bound Layer Meteor 48: 227–254

Whitaker JS, Uccellini LW, Brill KF (1988) A model-based diagnostic study of the rapid development phase of the Presidents' Day cyclone. Mon Wea Rev 116: 2337–2365

Zack JW, Kaplan ML (1987) Numerical simulations of the subsynoptic features associated with the AVE-SESAME I case study. Part I: The preconvective environment. Mon Wea Rev 115: 2367–2394

Corresponding author's address: S. Businger, Department of Meteorology, 2525 Correa Road, University of Hawaii, Honolulu, HI 96822 (E-mail: businger@soest.hawaii.edu)